Open access • Journal Article • DOI:10.1063/1.2013107

Ginzburg-Landau description of confinement and quantization effects in mesoscopic superconductors — Source link

Liviu F. Chibotaru, Arnout Ceulemans, Mathieu Morelle, Gerd Teniers ...+2 more authors

Published on: 29 Sep 2005 - Journal of Mathematical Physics (American Institute of Physics)

Topics: Neumann boundary condition, Ginzburg–Landau theory, Equilateral triangle, Regular polygon and Eigenvalues and eigenvectors

JOURNAL OF MATHEMATICAL PHYSICS **46**, 095108 (2005)

Ginzburg–Landau description of confinement and quantization effects in mesoscopic superconductors

L. F. Chibotaru and A. Ceulemans
Quantum Chemistry Group, Department of Chemistry, K. U. Leuven, Celestijnenlaan 200F, B-3001 Leuven, Belgium

M. Morelle, G. Teniers, C. Carballeira,[a] and V. V. Moshchalkov
Nanoscale Superconductivity and Magnetism Group, Department of Physics and Astronomy, K. U. Leuven, Celestijnenlaan 200 D, B-3001 Leuven, Belgium

(Received 22 June 2005; accepted 22 June 2005; published online 29 September 2005)

An approach to the Ginzburg–Landau problem for superconducting regular polygons is developed making use of an analytical gauge transformation for the vector potential $\mathbf{A}$ which gives $A_n=0$ for the normal component along the boundary line of different symmetric polygons. As a result the corresponding linearized Ginzburg–Landau equation reduces to an eigenvalue problem in the basis set of functions obeying Neumann boundary condition. Such basis sets are found analytically for several symmetric structures. The proposed approach allows for accurate calculations of the order parameter distributions at low calculational cost (small basis sets) for moderate applied magnetic fields. This is illustrated by considering the nucleation of superconductivity in squares, equilateral triangles and rectangles, where vortex patterns containing antivortices are obtained on the T_c–H phase boundary. The calculated phase boundaries are compared with the experimental $T_c(H)$ curves measured for squares, triangles, disks, rectangles, and loops. The stability of the symmetry consistent solutions against small deviations from the phase boundary line deep into the superconducting state is investigated by considering the full Ginzburg–Landau functional. It is shown that below the nucleation temperature symmetry-switching or symmetry-breaking phase transitions can take place. The symmetry-breaking phase transition has the same structure as the pseudo-Jahn-Teller instability of high symmetry nuclear configurations in molecules. The existence of these transitions is predicted to be strongly dependent on the size of the samples. © *2005 American Institute of Physics.* [DOI: 10.1063/1.2013107]

I. INTRODUCTION

"Confinement" and "quantization" are two closely related definitions: if a particle is "confined" then its energy is "quantized," and vice versa. According to the dictionary, to "confine" means to "restrict within limits," to "enclose," and even to "imprison." A typical example, illustrating the relation between confinement and quantization, is the restriction of the motion of a particle by enclosing it within an infinite potential well of size L_A.

Recent impressive progress in nanofabrication has made it possible to realize the whole range of confinement lengths L_A, from 1 μm (photo- and e-beam lithography), via 1 nm to 1 Å (single atom manipulation) and, through that, to control the confinement energy (temperature) from a few mK higher up to far above room temperature.

This progress has stimulated dramatically the experimental and theoretical studies of different

[a]On leave from Laboratorio de Baixas Temperaturas e Superconductividade, Departamento de Física da Materia Condensada, Universidade de Santiago de Compostela, E-15782 Santiago de Compostela, Spain.

nanostructured materials and individual nanostructures. The interest towards such structures arises from the remarkable principle of "quantum design," when quantum mechanics can be efficiently used to tailor the physical properties of nanostructured materials.

Modifying the sample topology in nanostructured materials creates a unique possibility to impose the desired boundary conditions, and through that to change the properties of the sample. A Fermi liquid or a superconducting condensate confined within such materials will be subjected to severe constraints and, as a result, the properties of these materials will be strongly affected by the boundary conditions.[1]

While a normal metallic system should be considered quantum mechanically by solving the Schrödinger equation:

$$\frac{1}{2m}(-\imath\hbar\vec{\nabla}-e\vec{A})^2\Psi+U\Psi=E\Psi, \tag{1}$$

a superconducting system is described by the two coupled Ginzburg–Landau (GL) equations,[2]

$$\frac{1}{2m^\star}(-i\hbar\vec{\nabla}-e^\star\vec{A})^2\Psi_s+\beta|\Psi_s|^2\Psi_s=-\alpha\Psi_s, \tag{2}$$

$$\vec{j}=\vec{\nabla}\times\vec{h}=\frac{e^\star}{2m^\star}[\Psi_s^\star(-\imath\hbar\vec{\nabla}-e^\star\vec{A})\Psi_s+\Psi_s(\imath\hbar\vec{\nabla}-e^\star\vec{A})\Psi_s^\star], \tag{3}$$

with $\vec{A}$ the vector potential which corresponds to the microscopic field $\vec{h}=\mathrm{rot}\,\vec{A}/\mu_0$, U the potential energy, E the total energy, α a temperature dependent parameter changing sign from $\alpha>0$ to $\alpha<0$ as T is decreased through T_c, β a positive temperature independent constant, $m^\star$ the effective mass which can be chosen arbitrarily and is generally taken as twice the free electron mass m.

Note that the first GL equation [Eq. (2)], with the nonlinear term $\beta|\Psi_s|^2\Psi_s$ neglected, is the analogue of the Schrödinger equation [Eq. (1)] with $U=0$, when making a few substitutions, $\Psi_s\leftrightarrow\Psi$, $e^\star\leftrightarrow e$, $-\alpha\leftrightarrow E$, and $m^\star\leftrightarrow m$. The superconducting order parameter Ψ_s corresponds to the wave function Ψ in Eq. (1). The effective charge $e^\star$ in the GL equations is $2e$, i.e., the charge of a Cooper pair, while the temperature dependent GL parameter α,

$$-\alpha=\frac{\hbar^2}{2m^\star\xi^2(T)}, \tag{4}$$

plays the role of E in the Schrödinger equation. Here $\xi(T)$ is the temperature dependent coherence length,

$$\xi(T)=\frac{\xi(0)}{\sqrt{1-\dfrac{T}{T_{c0}}}}. \tag{5}$$

The boundary conditions for interfaces normal metal vacuum and superconductor vacuum are, however, different,[3]

$$\Psi\Psi^\star|_b=0, \tag{6}$$

$$(-\imath\hbar\vec{\nabla}-e^\star\vec{A})\Psi_s|_{\perp,b}=0, \tag{7}$$

i.e., for normal metallic systems *the density* is zero at the boundary (Dirichlet boundary condition), while for superconducting systems, *the current density* has no component perpendicular to the boundary. As a consequence, the supercurrent cannot flow through the boundary. The nucleation of the superconducting condensate is favored at the superconductor/vacuum interfaces, thus leading

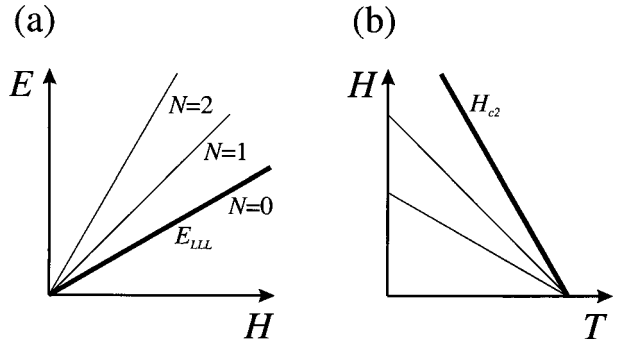

FIG. 1. Landau level scheme in the bulk. From the lowest Landau level $E_{\mathrm{LLL}}(H)=\hbar\omega/2$ [panel (a)] the second critical field $H_{c2}(T)$ [panel (b)] is derived.

to the appearance of superconductivity, at the third critical field $H_{c3}(T)$, in a surface sheet with a thickness $\xi(T)$.

For bulk superconductors the surface-to-volume ratio is negligible and therefore superconductivity in the bulk is not affected by a thin superconducting surface layer. For nanostructured superconductors with antidot arrays, however, the boundary conditions [Eq. (7)] and the surface superconductivity introduced through them become very important if $L_A \leqslant \xi(T)$. The advantage of superconducting materials in this case is that it is not even necessary to go to nm scale (like for normal metals), since for L_A of the order of 0.1–1.0 μm the temperature range where $L_A \leqslant \xi(T)$, spreads over 0.01–0.1 K below T_c due to the divergence of $\xi(T)$ at $T \to T_{c0}$ [Eq. (5)].

In principle, the mesoscopic regime $L_A \leqslant \xi(T)$ [and $L_A \leqslant \lambda(T)$, with λ the magnetic penetration depth] can eventually be reached even in bulk superconducting samples with $L_A \sim 1$ cm^{-1} m, since $\xi(T)$ [and $\lambda(T)$ as well] diverges at $T \to T_{c0}$. However, the temperature window where $L_A \leqslant \xi(T)$ is so narrow, not more than ~ 1 nK below T_{c0}, that one needs ideal sample homogeneity and perfect temperature stability.

In the mesoscopic regime $L_A \leqslant \xi(T)$, which is quite easily realized in nanostructured materials, the surface superconductivity can cover the whole available space occupied by the material, thus spreading superconductivity all over the sample. It is then evident that in this case the surface effects play the role of bulk effects.

Using the similarity between the linearized GL equation [Eq. (2)] and the Schrödinger equation [Eq. (1)], the approach to determine $T_c(H)$ can be formalized as follows: since the parameter $-\alpha$ [Eqs. (2) and (4)] plays the role of energy E [Eq. (1)], then *the highest possible temperature $T_c(H)$ for the nucleation of the superconducting state in presence of the magnetic field H always corresponds to the lowest Landau level $E_{\mathrm{LLL}}(H)$* found by solving the Schrödinger equation [Eq. (1)] with "superconducting" boundary conditions [Eq. (7)].

Figure 1 illustrates the application of this basic rule to the calculation of the upper critical field $H_{c2}(T)$, indeed, if the well-known classical Landau solution for the lowest level in a bulk sample $E_{\mathrm{LLL}}(H)=\hbar\omega/2$, where $\omega=e^{\star}\mu_0 H/m^{\star}$ is the cyclotron frequency, is taken, then, from $-\alpha = E_{\mathrm{LLL}}(H)$, we have

$$\frac{\hbar^2}{2m^{\star}\xi^2(T)} = \frac{\hbar\omega}{2}\bigg|_{H=H_{c2}} \tag{8}$$

with the help of Eq. (4). We obtain

$$\mu_0 H_{c2}(T) = \frac{\Phi_0}{2\pi\xi^2(T)}, \tag{9}$$

with $\Phi_0 = h/e^{\star} = h/2e$ the superconducting flux quantum.

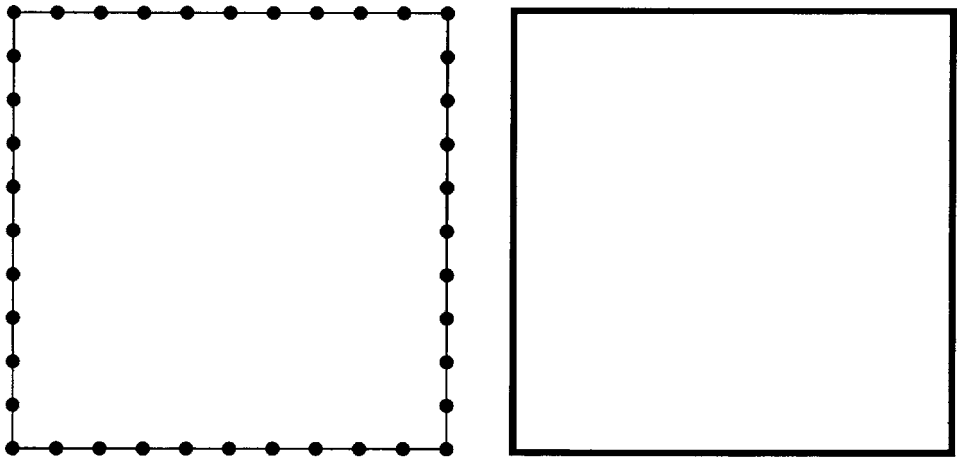

FIG. 2. Domains (bold dots and lines) of the boundary line where the condition in Eq. (7) is satisfied exactly for the case of finite grid (a) and appropriate vector potential gauge (b) methods.

In nanostructured superconductors, where the boundary conditions [Eq. (7)] strongly influence the Landau level scheme, $E_{\mathrm{LLL}}(H)$ must be calculated for each specific confinement geometry. By measuring the shift of the critical temperature $T_c(H)$ in a magnetic field, one can compare the experimental phase boundary $T_c(H)$ with the calculated level $E_{\mathrm{LLL}}(H)$ and thus check the effect of the confinement topology on the superconducting phase boundary for a series of nanostructured superconducting samples. The transition between normal and superconducting states is usually very sharp and therefore the lowest Landau level can be easily traced as a function of applied magnetic field. The midpoint of the resistive transition from the superconducting to the normal state is usually taken as the criterion to determine $T_c(H)$.

This defines the main strategy of our paper to use systematically the GL approach to calculate the condensate density and the energy levels [including $E_{\mathrm{LLL}}(H)$ for superconducting samples of different geometries and topologies and to compare the calculated lowest level $E_{\mathrm{LLL}}(H)$] with the measured $T_c(H)$ phase boundary.

The presence of the vector potential in the boundary condition, Eq. (4), seriously complicates the solution of the Ginzburg–Landau equations for samples of arbitrary geometry. Existing treatments use numerical methods like the method of finite differences. This way proved to be successful for the description of superconductivity in mesoscopic structures[4,5] although it is usually achieved at the expense of high computational costs. The problem, however, simplifies very much if one can find a gauge for the vector potential ($\widetilde{\mathbf{A}}$) giving zero normal component on the boundary line

$$\widetilde{\mathbf{A}}|_n = 0. \tag{10}$$

In these cases the superconducting boundary condition in Eq. (7) reduces to the Neumann boundary condition,

$$\nabla\Psi|_n = 0, \tag{11}$$

which is much easier to satisfy. Such gauges have been found in the past for infinite slabs,[6] semiplanes with a wedge,[7,8] and disks.[9–12]

The major difference between the above approaches is the extent to which they fulfill the superconducting boundary condition. As Fig. 2 shows, the method of finite differences satisfies Eq. (7) only on a finite set of points along the boundary line, while by using an appropriate gauge for the vector potential (10) we are able *to satisfy the boundary condition everywhere on the*

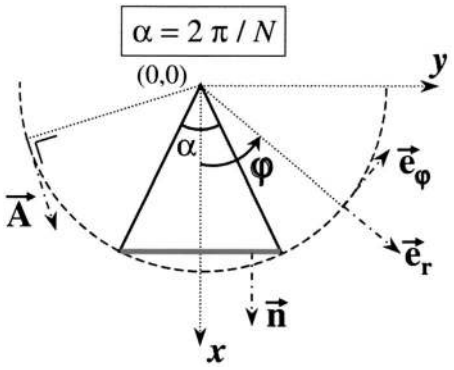

FIG. 3. Piece of a regular polygon containing one edge (thick line). The origin of the coordinate system is chosen in the center of the polygon. $\mathbf{n}$ is the unit vector normal to the edge. $\mathbf{e}_r$ and $\mathbf{e}_\varphi$ are unit vectors of the cylindrical coordinate system. The z axis coincides with the N fold rotational axis of the polygon.

boundary. Since Eq. (7) is nothing but a sort of quantization condition for our problem, we can conclude that finite grid methods always imply an *approximate* solution of Eq. (7), while the methods using the appropriate gauge for the vector potential treat it *exactly*. This is crucial for the proper description of the order parameter in the cases when the boundary becomes important, i.e., for low values of the applied flux.

In this paper we review the development of this second type of approach to the Ginzburg–Landau problem for symmetric superconducting polygons in external magnetic field. In Secs. II and III we present the derivation of vector potential gauge and the basis set for several symmetric structures. The application of this approach to the description of the nucleation of superconductivity in different polygons is given in Sec. IV. Here the evolution of the vortex patterns as a function of applied magnetic field is investigated in detail. We also compare the calculated superconducting/normal phase boundary lines with the experimental ones. The evolution from a disk to thin loops is discussed in Sec. V. In Sec. VI we study the stability of the LGL solutions corresponding to nucleated phases and the conditions for the arising of different phase transitions when the temperature is lowered from the nucleation point. Finally Sec. VII gives some conclusions and the perspective for the future work.

II. VECTOR POTENTIAL GAUGE FOR SYMMETRIC POLYGONS

Consider a regular polygon with N edges. It has a symmetry axis of order N, corresponding to rotations by angles which are multiples of $2\pi/N$. An external homogeneous magnetic field applied along this axis can be described by a vector potential

$$\mathbf{A} = \tfrac{1}{2}\mathbf{H} \times \mathbf{r}, \tag{12}$$

where the radius vector lies in the xy plane (Fig. 3) and $\mathbf{H} \| \mathbf{z}$. Equation (12) defines the cylindrical gauge for $\mathbf{A}$. It is often preferred over many other possible choices[13] due to the high symmetry which allows to preserve the rotational symmetry of the system without field. The direction of $\mathbf{A}$ is tangential to concentric circumferences, $\mathbf{A} \| \mathbf{e}_\varphi$, which are also equipotential lines for the vector potential.

As one can see from Fig. 3, the vector potential in Eq. (12) is not tangential to the boundary line (i.e., the edges) of a polygon. On the edge shown in Fig. 3 it contains a normal component

$$A_n(\varphi) = -C \tan \varphi,$$

$$C = \tfrac{1}{4} H\, a, \tag{13}$$

where φ is the polar angle and a is the diameter of the circumference inscribed in the regular polygon. Our purpose is to find a new vector potential which would be tangential to the edges. This can be done by the following gauge transformation:[13]

$$\tilde{\mathbf{A}} = \mathbf{A} + \nabla S, \tag{14}$$

where $\mathbf{A}$ is the old and $\tilde{\mathbf{A}}$ is the new vector potential and S is an arbitrary scalar function. This function is found from the condition $\tilde{A}_n = 0$ on the boundary line. This is equivalent to the equation

$$A_n = -\nabla_n S, \tag{15}$$

which must be obeyed on each edge. In order to keep the rotational symmetry of the regular polygon $\tilde{\mathbf{A}}$ and S should be periodic functions of φ with the period α (Fig. 3). Because $\tilde{\mathbf{A}}$ is real, this suggests the following general form for S (in polar coordinates):

$$S(r,\varphi) = \sum_m [R_m^s(r)\sin(Nm\varphi) + R_m^c(r)\cos(Nm\varphi)], \tag{16}$$

where m are non-negative integers. Due to the rotational periodicity of the function S it is enough to satisfy Eq. (15) on one single edge. The form in Eq. (16) is further simplified due to the symmetry requirement that $\tilde{\mathbf{A}}$ is purely tangential on the radial lines defined by $\varphi = \pm\alpha/2$ and $\varphi = 0$ (Fig. 3). The latter requirement means that ∇S is purely tangential on the radial line $\varphi = 0$ which can only be the case if one takes $R_m^c(r) = 0$ in Eq. (16).

Next we simplify the remaining part of the form (16) by confining ourselves to one single term in the summation. Obviously this cannot be the term $m = 0$ because ∇S should be dependent on φ as it is easily seen from Eqs. (13) and (15). Therefore the simplest possible term is $m = 1$ which leads to the ansatz,

$$S_N(r,\varphi) = R_N(r)\sin(N\varphi). \tag{17}$$

Substituting Eqs. (13) and (17) into (15), after eliminating the r variable on the edge line,

$$r = \frac{a}{2\cos\varphi},$$

$$\frac{\partial}{\partial r} = \frac{2}{a}\frac{\cos^2\varphi}{\sin\varphi}\frac{\partial}{\partial\varphi}, \tag{18}$$

one obtains the following equation in φ:

$$\tilde{R}_N' \sin(N\varphi)\cos^2\varphi - \tilde{R}_N \sin(N\varphi)'\sin^2\varphi = \tan^2\varphi, \tag{19}$$

where the prime in the superscript means the first derivative after φ and the following notation was introduced:

$$\tilde{R}_N(\varphi) = \frac{2}{aC} R_N\left(\frac{a}{2\cos\varphi}\right). \tag{20}$$

Bringing Eq. (19) to the form

$$\tilde{R}_N' + \xi(\varphi)\tilde{R}_N = \eta(\varphi), \tag{21}$$

where

$$\xi(\varphi) = -N\cot(N\varphi)\tan^2\varphi,$$

$$\eta(\varphi) = \csc(N\varphi)\tan^2\varphi/\cos^2\varphi, \tag{22}$$

allows us to write down the general solution[14]

$$\widetilde{R}_N(\varphi) = \frac{1}{\mu(\varphi)}\left(\int \eta(\varphi)\mu(\varphi)\mathrm{d}\varphi + C_1\right),$$

$$\mu(\varphi) = \exp\left(\int \xi(\varphi)\mathrm{d}\varphi\right). \tag{23}$$

The solution (23) describes the radial function in Eq. (17) only for values of r which are radius vectors of the points on the edge's line. One can extend this solution over the whole range of r by the inverse transformation to (18), $a/2\cos\varphi \to r$. Then using again Eqs. (14), (17), and (20) we can express the polar components of the gauge transformed vector potential $\widetilde{\mathbf{A}}$,

$$\widetilde{A}_r = \frac{\partial R_N(r)}{\partial r}\sin(N\varphi),$$

$$\widetilde{A}_\varphi = \frac{1}{2}Hr + \frac{N}{r}R_N(r)\cos(N\varphi), \tag{24}$$

through the solution (23). The constant C_1 contained in that solution should be chosen in such a way as to provide nondivergent components of the vector potential (24). In contrast to $\mathbf{A}$ in Eq. (12), the vector potential defined by Eqs. (24) does not obey the Coulomb gauge, $\nabla\cdot\mathbf{A}=0$. Hence the term $\nabla\cdot\mathbf{A}$ plays the role of a scalar potential in a Hamiltonian and should be nondivergent either. Fortunately both requirements are met within the area of the polygon under the simple condition $C_1=0$.

Analytical expressions of Eqs. (23) for some regular polygons are given in Ref. 15.

In the case of equilateral triangle the solutions (24) have the form

$$\widetilde{A}_r = \tfrac{27}{2}Ha\left(9r'^8 - 7r'^6 + \tfrac{5}{3}r'^4\right)\sin 3\varphi,$$

$$\widetilde{A}_\varphi = \tfrac{1}{2}Hr + \tfrac{81}{2}Ha\left(r'^8 - r'^6 + \tfrac{1}{3}r'^4\right)\cos 3\varphi,$$

$$r' = r/\sqrt{3}a, \tag{25}$$

where a is the side length of the triangle. Figure 4 shows how the gauge transformed vector potential looks for the equilateral triangle. We can see that it gradually changes from the cylindrical gauge in the central region to a triangular pattern close to the edges. According to this gauge transformation one should add to Eq. (4) the following divergency term:

$$\nabla\cdot\widetilde{\mathbf{A}} = H\frac{9\sqrt{3}}{2}\left(72r'^7 - 40r'^5 + \frac{16}{3}r'^3\right)\sin 3\varphi. \tag{26}$$

In the case of a square the solutions of Eqs. (23) and (24) yield the following gauge transformed vector potential (Fig. 5):

$$\widetilde{A}_r = -\frac{1}{4\sqrt{2}}Ha(1+u)^{3/2}[-1+u+(1+2u-u^2)e^{-u}Ei(u)]\sin 4\varphi,$$

$$\widetilde{A}_\varphi = \frac{1}{2}Hr + \frac{1}{2\sqrt{2}}Ha(1+u)^{3/2}[1-ue^{-u}Ei(u)]\cos 4\varphi,$$

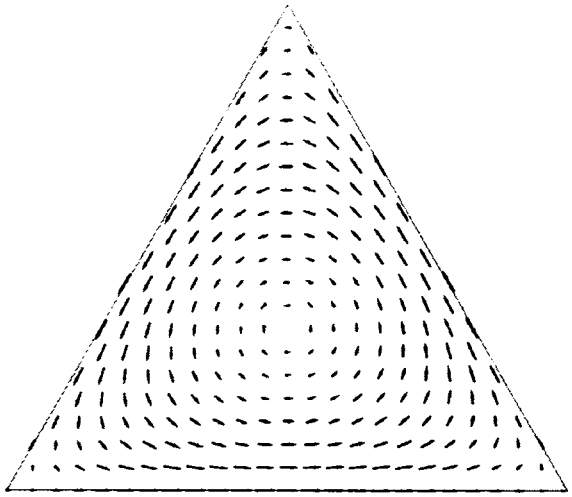

FIG. 4. Vector potential for the equilateral triangle (arbitrary units) after the gauge transformation, described by Eqs. (25).

$$u = 2(r/a)^2 - 1, \tag{27}$$

where $Ei(u)$ is the exponential integral function[16] and a is the side length of the square. In full analogy with the previous case (Fig. 4), this vector potential coincides with the cylindrical gauge in the central region and smoothly changes into a square symmetry pattern when approaching the boundaries. The corresponding divergency term is obtained as follows:

$$\boldsymbol{\nabla} \cdot \tilde{\mathbf{A}} = H\frac{(1+u)^2}{2u}[-1-5u+u^2-u(3-6u+u^2)e^{-u}Ei(u)]\sin 4\varphi. \tag{28}$$

The results for the square are easily extended over arbitrary rectangles, described by the aspect

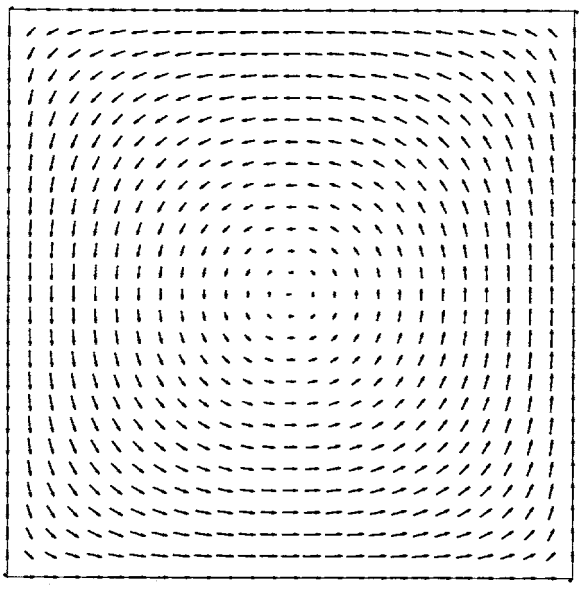

FIG. 5. Vector potential for the square (arbitrary units) after the gauge transformation, described by Eqs. (27).

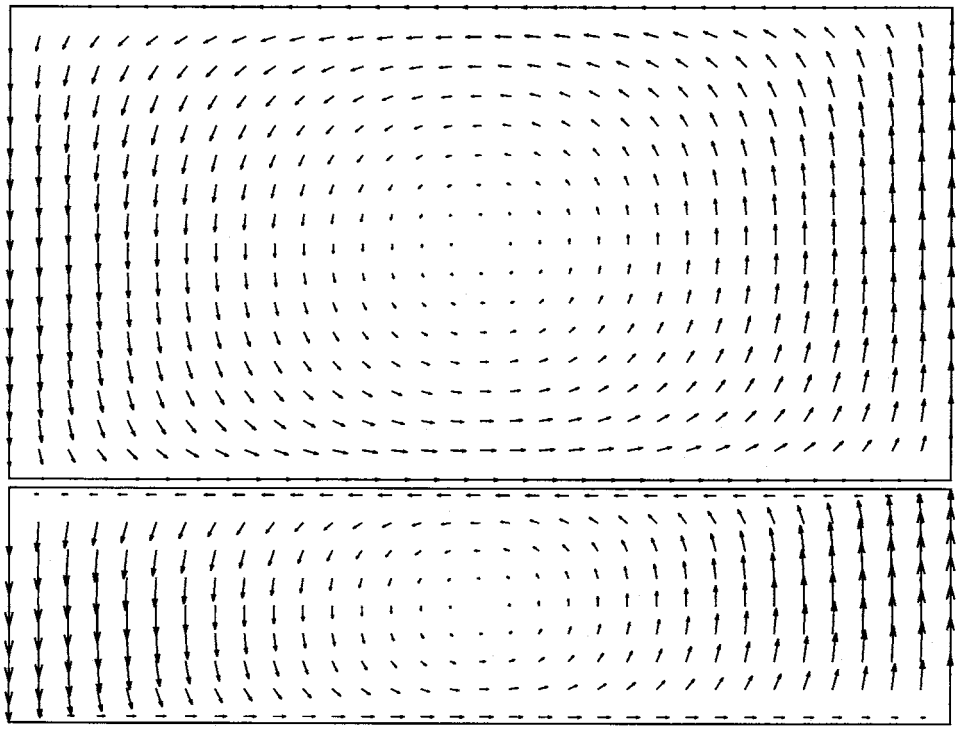

FIG. 6. Vector potential for the rectangle (arbitrary units) with aspect ratio two (top) and four (bottom) after the gauge transformation, described by Eqs. (14), (27), and (29).

ratios $\zeta=a/b$, where a and b are the lengths of the two sides. Directing the Cartesian axes x and y along the sides a and b, respectively, we find the following relation for the scalar function S entering the gauge transformed vector potential (14) for the rectangle:

$$S_{\mathrm{rect}}(x,y) = S_{\mathrm{sq}}\left(\frac{1}{\sqrt{\zeta}}x, \sqrt{\zeta}y\right), \tag{29}$$

where S_{sq} is the scalar function for the square with the side length $a/\sqrt{\zeta}=\sqrt{\zeta}b$. After substitution of Eq. (29) into (14), written in polar coordinates, we can make direct use of Eqs. (27). The resulting gauge transformed vector potential is shown in Fig. 6. The divergency term to be inserted into Eq. (4) is just ΔS_{rect}.

Another extension of the above approach concerns symmetric nonhomogeneous applied magnetic fields. These can be induced, for instance, by setting a cylindrical quantum dot uniformly magnetized along its axis on the top of a superconducting sample.[17,18] This magnetic field together with an independent homogeneous component corresponds to a vector potential of cylindrical symmetry[19]

$$A_{\varphi}(r) = \frac{1}{2}Hr + 4M\sqrt{\frac{R}{r}}\int_0^l \frac{\left[\left(1-\frac{k^2}{2}\right)K(k) - E(k)\right]}{k}\mathrm{d}z,$$

$$k^2 = \frac{4rR}{(r+R)^2+z^2}, \tag{30}$$

where R, l, and M are the radius, the height, and the density of magnetization of the cylindrical dot, respectively; K and E are elliptic integrals of first and second kind, respectively, and H is the

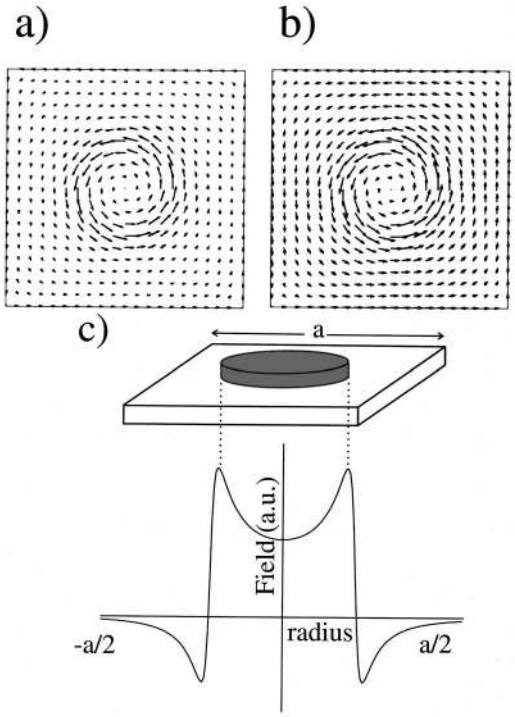

FIG. 7. Vector potential for a square with cylindrical uniformly magnetized quantum dot (a) in an external homogeneous magnetic field producing one flux quantum in the sample, (b) in zero external field. The dot has a radius 0.2 times and a height 0.032 times the sample size a and the magnetization produces one flux quantum in the sample. (c) Schematic drawing of the superconducting square with the magnetic dot (gray) and the corresponding field profile.

intensity of the homogeneous magnetic field as before. Repeating all derivations with the new applied vector potential (30) instead of the cylindrical one (12) we obtain similar results as in Eqs. (22), (23), and (24), where the second equation from (22) should be replaced by

$$\eta(\varphi) = \csc(N\varphi)\frac{\tan^2\varphi}{\cos\varphi}A_\varphi\left(\frac{a}{2\cos\varphi}\right), \tag{31}$$

and A_φ should replace $Hr/2$ in the second equation of (24). However now we can no longer find the primitive in the first equation of (23) in analytical form. This complication can be avoided if we approximate the function $A_\varphi(r)$ by polynomials. This can be done for arbitrary parameters of the dot, which allows to obtain the explicit expressions for the components of the gauge transformed vector potential.[20] Figure 7 shows the gauge transformed vector potential for a square with a cylindrical magnetic dot on top of it. We can see that the behavior of $\tilde{\mathbf{A}}$ as function of r is similar to the previous cases.

III. BASIS SET FOR THE GL PROBLEM OF SYMMETRIC POLYGONS

Having found a gauge for the vector potential ($\tilde{\mathbf{A}}$) satisfying the condition (10) on the boundary line, it follows immediately from Eq. (7) that the order parameter can be expanded into a set of functions, $\{\psi_m\}$,

$$\Psi = \sum_m c_m\psi_m, \tag{32}$$

obeying the Neumann boundary condition,

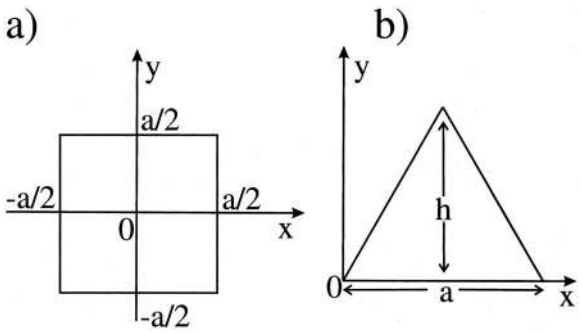

FIG. 8. Coordinate systems used in the derivation of the basis set for a square (a) and an equilateral triangle (b).

$$\nabla \psi_m|_n = 0. \tag{33}$$

For calculational convenience the functions ψ_m are supposed to form an orthonormal set. Furthermore, in order to reduce the dimension of the basis set these functions should be as close as possible to the expected solutions of Eq. (4). Since we are interested in solutions for moderate values of applied magnetic fluxes both requirements are met for sets of low-lying eigenfunctions of the zero-field (i.e., particle in the polygonal box) eigenvalue problem,

$$-\frac{\hbar^2}{2m^*}\Delta\psi_m = \epsilon_m \psi_m, \tag{34}$$

obeying the boundary condition (33).

Consider a regular polygon shaped sample of a constant width in a homogeneous magnetic field applied along the direction perpendicular to the polygonal surface ($\mathbf{H}\|\mathbf{z}$). Then the associated vector potential $\mathbf{A}$ is directed in the xy plane (see Fig. 3). Since $A_z=0$ and the other two components depend on x and y only, the solution of Eq. (34) factorizes as $\Psi(x,y)\Phi(z)$. The z-dependent component of the solution satisfying the boundary condition $d\Phi/dz=0$, $z=\pm d/2$, and corresponding to the lowest value of $-\alpha$ in Eq. (4) has the form $\Phi=$const. This means that the superconductivity nucleates homogeneously across the width of the sample and the solution of the LGL equation reduces to a two-dimensional (2D) problem.

The transformation (14) and (17) keeps the symmetry of the vector potential [and of Eqs. (4)] equal to the rotational symmetry of the sample, described by the point group C_N. Since the LGL equation is a linear eigenvalue problem its solutions, according to Wigner's theorem,[21] are characterized by irreducible representations (irreps) of the corresponding symmetry group. The point group C_N is Abelian and therefore contains N different one-dimensional irreps which transform as

$$\psi_n(\varphi) \sim \exp(in\varphi),$$

$$n = 0,1,\ldots,N-1, \tag{35}$$

under rotations around the z axis by symmetry angles, the smallest of which coincides with the angle α in Fig. 3. The symmetry analysis provides a set of N labels to assign eigenfunctions and splits the matrix eigenvalue equation into diagonal blocks corresponding to different irreps[21] which simplifies the calculations.

A. Square and rectangle

In these geometries the boundary conditions allow the separation of variables in the eigenvalue problem (34) if one chooses the coordinate axes parallel to corresponding edges [Fig. 8(a)].

Along each coordinate the problem reduces to a particle in the box with infinite potential walls.[21] The corresponding solution for the boundary conditions (33) has the form (l is the dimension of the box)

$$\psi_k^1(x) = \sqrt{\frac{2}{l}}\cos kx, \quad k = \frac{2n\pi}{l},$$

$$\psi_k^2(x) = \sqrt{\frac{2}{l}}\sin kx, \quad k = \frac{(2n+1)\pi}{l},$$

$$n = 0,1,2,\ldots . \tag{36}$$

The full solutions in a rectangular box are just the products $\psi_{k_x}(x)\psi_{k_y}(y)$ and correspond to the energy,

$$E_{k_xk_y} = \frac{\hbar^2(k_x^2+k_y^2)}{2m^*}. \tag{37}$$

These solutions however do not correspond to any definite symmetry. Therefore they should be symmetrized if we want to take advantage of the symmetry of the samples as discussed above.

A *square* in homogeneous magnetic field has the symmetry described by the rotational point group C_4, which contains the irreps A, B, E_+, and E_- with the corresponding numbers $n=0$, 2, 1, and -1 (or 3) in Eq. (35). Using the conventional symmetry projection technique[21] the symmetrized basis set is easily constructed from the solutions in Eq. (37). Thus we obtain the following types of solutions, for the irrep A:

$$\psi_A^1 = \frac{\sqrt{2}}{a}[\cos k_1x\cos k_2y + \cos k_2x\cos k_1y],$$

$$k_1 > k_2 \geqslant 0, \quad k_i = \frac{2n_i\pi}{a},$$

$$\psi_A^2 = \frac{2}{a}\cos kx\cos ky, \quad k = \frac{2n\pi}{a} \geqslant 0,$$

$$\psi_A^3 = \frac{\sqrt{2}}{a}[\sin k_1x\sin k_2y - \sin k_2x\sin k_1y],$$

$$k_1 > k_2 > 0, \quad k_i = \frac{(2n_i+1)\pi}{a}, \tag{38}$$

for the irrep B,

$$\psi_B^1 = \frac{\sqrt{2}}{a}[\cos k_1x\cos k_2y - \cos k_2x\cos k_1y],$$

$$k_1 > k_2 \geqslant 0, \quad k_i = \frac{2n_i\pi}{a},$$

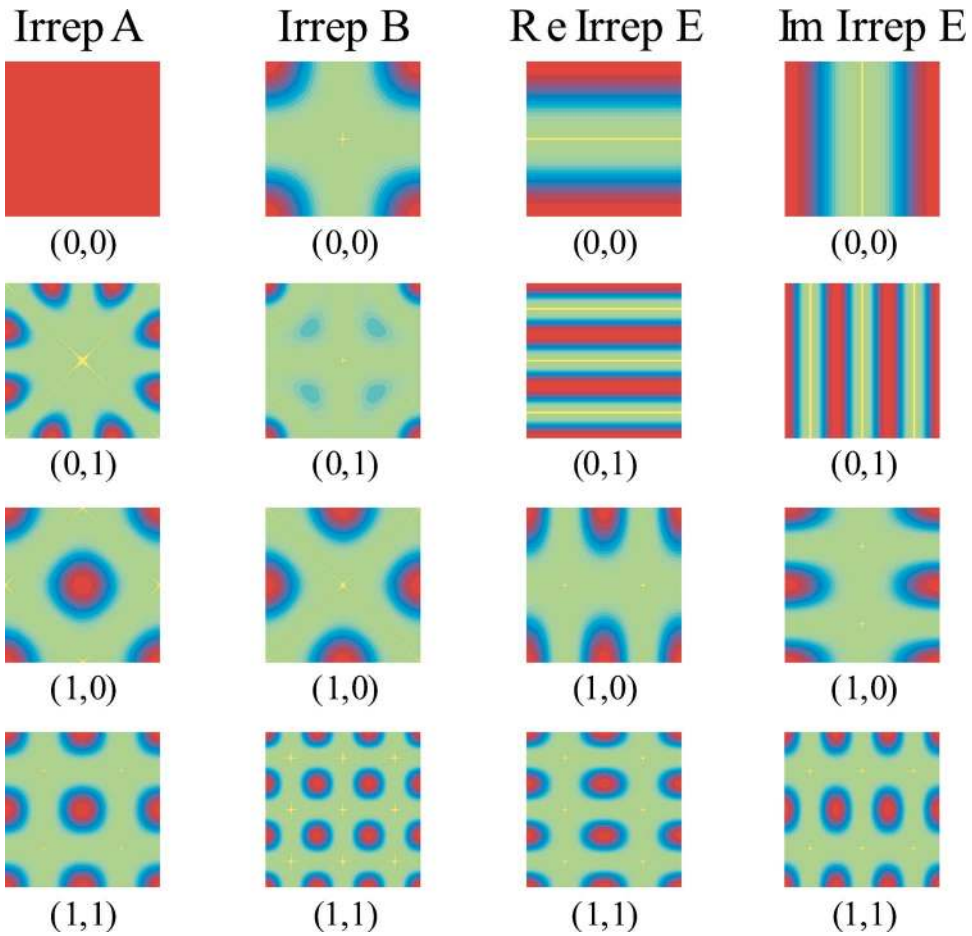

FIG. 9. (Color online) Symmetrized basis functions for a square. The highest density is shown in darker shades and the lowest $|\psi|^2$ values are lighter shades. The numbers in parentheses stand for n_1 and n_2, respectively.

$$\psi_B^2 = \frac{2}{a}\sin kx \sin ky, \quad k = \frac{(2n+1)\pi}{a} > 0,$$

$$\psi_B^3 = \frac{\sqrt{2}}{a}[\sin k_1 x \sin k_2 y + \sin k_2 x \sin k_1 y],$$

$$k_1 > k_2 > 0, \quad k_i = \frac{(2n_i+1)\pi}{a} \tag{39}$$

and for the irrep E,

$$\psi_{E_{+,-}} = \frac{\sqrt{2}}{a}[\cos k_1 x \sin k_2 y \pm i \cos k_1 y \sin k_2 x],$$

$$k_1 = \frac{2n_1\pi}{a} \geqslant 0, \quad k_2 = \frac{(2n_2+1)\pi}{a} \geqslant 0, \tag{40}$$

where n_i are integers. Figure 9 shows graphically some of these symmetrized functions.

In a *rectangle* the symmetry in homogeneous magnetic field is described by the point group

C_2 containing only two irreps, A and B. The reduction of symmetry with respect to the square induces the following reduction of the irreps of C_4: $A,B\rightarrow A$, $E_+,E_-\rightarrow B$. The basis function resulting from this reduction have the following form, for irrep A:

$$\psi_A^1=\frac{2}{\sqrt{ab}}\cos k_1x\cos k_2y,$$

$$k_1=\frac{2n_1\pi}{a},\quad k_2=\frac{2n_2\pi}{b},$$

$$\psi_A^2=\frac{2}{\sqrt{ab}}\sin k_1x\sin k_2y,$$

$$k_1=\frac{(2n_1+1)\pi}{a},\quad k_2=\frac{(2n_2+1)\pi}{b}, \tag{41}$$

and for the irrep B,

$$\psi_B^1=\frac{2}{\sqrt{ab}}\cos k_1x\sin k_2y,$$

$$k_1=\frac{2n_1\pi}{a},\quad k_2=\frac{2(n_2+1)\pi}{b},$$

$$\psi_B^2=\frac{2}{\sqrt{ab}}\sin k_1x\cos k_2y,$$

$$k_1=\frac{(2n_1+1)\pi}{a},\quad k_2=\frac{2n_2\pi}{b} \tag{42}$$

where n_i are integers.

B. Equilateral triangle

This case is more involved since the geometry of the boundary does not allow the separation of variables in the eigenvalue problem (34). Nevertheless it is still possible to express the solutions as a linear combination of a small number ($\leqslant 6$) of plane waves as shown below.

The equilateral triangle in a homogeneous magnetic field has a symmetry corresponding to the rotational point group C_3, which contains the irreps A, E_+, and E_- matching the numbers $n=0$, 1, and -1 (or 2) in Eq. (35), respectively. We make use of this symmetry in the next section when we analyze the solutions of the corresponding LGL equation. The particle in the box problem, however, is characterized by a higher symmetry group C_{3v}, containing in addition three vertical reflection planes, which are absent when the magnetic field is applied. It is convenient to use this higher symmetry group in further derivation. The method used here follows closely the one employed by Li and Blinder for a triangular box with Dirichlet boundary conditions.[22] For an equilateral triangle located with respect to Cartesian axes as shown in Fig. 8(b) we introduce three variables (h is the height of the triangle),

$$u=\frac{2\pi}{h}y,$$

$$v = \frac{2\pi}{h}\left(-\frac{1}{2}y + \frac{\sqrt{3}}{2}x\right),$$

$$w = \frac{2\pi}{h}\left(-\frac{1}{2}y - \frac{\sqrt{3}}{2}x\right) + 2\pi, \tag{43}$$

which are obviously linearly dependent. These variables are transformed into each other under symmetry operations of the C_{3v} group and obey simple relations on the boundaries of the triangle. For instance, on the edge $y=0$ [Fig. 8(b)] we have

$$u = 0, \quad v = 2\pi - w. \tag{44}$$

Equation (34) is satisfied for a harmonic function with arbitrary linear combination of x and y in the argument. It is convenient to take this function in the form $f(pu-qv)$,[22] where u and v are variables introduced in Eq. (43), corresponding to the energy (in units of $\hbar^2/2m^*$),

$$E_{pq} = 4\frac{\pi^2}{h^2}(p^2 + pq + q^2). \tag{45}$$

Starting from the function f, we construct wave functions of definite symmetry by using the method of symmetry projection.[21] The projected functions are linear combinations of functions f of different arguments, all of which obviously correspond to the same energy (45). Due to this symmetrization it is enough to satisfy the boundary condition (33) on a single edge, e.g., $y=0$ [Fig. 8(b)]. Equation (44) shows that on that boundary the wave function depends on a single variable v. The boundary condition is then satisfied by choosing appropriate values of the constants p and q which, at their turn, define the allowed values of the energy (45).

Irrep A_1: The boundary condition at the edge $y=0$ is obtained in the form

$$\left.\frac{\partial \psi_{A_1}}{\partial u}\right|_{u=0} = (2p+q)(f'_u[-qv] + f'_u[qv - 2\pi q]) + (-p+q)(f'_u[-(p+q)v + 2\pi p] + f'_u[(p+q)v - 2\pi q]) - (p+2q)(f'_u[-pv + 2\pi p] + f'_u[pv]) = 0. \tag{46}$$

Since f is a harmonic function with the period 2π, the above equation is only satisfied for integer values of p and q and $f=\cos$. Furthermore, the function ψ_{A_1} is invariant under the following replacements of the two constants: $p,q \to q,p$, $p,q \to -p,-q$ and $p+q,-p \to p,q$. This restricts p and q to positive values. Rewriting this function in x and y variables we obtain (without normalization)

$$\psi^{A_1}_{pq}(x,y) = \cos\frac{\pi}{h}(2p+q)y \cos\frac{\pi}{h}\sqrt{3}qx + \cos\frac{\pi}{h}(-p+q)y \cos\frac{\pi}{h}\sqrt{3}(p+q)x + \cos\frac{\pi}{h}(p+2q)y \cos\frac{\pi}{h}\sqrt{3}px,$$

$$p \geqslant q = 0,1,2,\ldots . \tag{47}$$

Irrep A_2: The boundary conditions for ψ_{A_2} lead to an equation similar to (46) with the only difference that now differences of derivatives f'_u enter in each of the square brackets instead of their sum. This means that the only choice for the harmonic function is $f=\sin$. The constants p and q are again integers and obey the same symmetry relations as in the previous case. Therefore, we obtain for the irrep A_2 the following unnormalized eigenfunctions:

$$\psi_{pq}^{A_2}(x,y) = -\sin\frac{\pi}{h}\sqrt{3}qx\cos\frac{\pi}{h}(2p+q)y + \sin\frac{\pi}{h}\sqrt{3}(p+q)x\cos\frac{\pi}{h}(-p+q)y$$
$$-\sin\frac{\pi}{h}\sqrt{3}px\cos\frac{\pi}{h}(p+2q)y,$$

$$p \geqslant q = 1,2,\ldots . \tag{48}$$

Note that in the presence of homogeneous magnetic field both ψ_{A_1} and ψ_{A_2} reduce to the same irrep A of the group C_3.

Irrep E: Because this irrep is twofold degenerate the corresponding two eigenfunctions are defined up to an arbitrary linear combination. It is convenient to choose these functions as complex conjugate to each other because then they belong automatically to the irreps E_+ and E_- of the group C_3, respectively. This requirement leaves us the only choice for the harmonic function, $\exp[i(pu-qv)]$. After similar derivations as in previous cases we obtain for the unnormalized eigenfunctions $[\psi^{E-}=(\psi^{E+})^*]$

$$\psi_{pq}^{E-}(x,y) = \exp\left\{\frac{\pi i}{h}[(2p+q)y-\sqrt{3}qx]\right\} + \exp\left\{\frac{\pi i}{h}[(p+2q)y-\sqrt{3}px]\right\}$$
$$+\exp\left\{\frac{\pi i}{h}[(-p+q)y+\sqrt{3}(p+q)x]-2\pi qi \pm \frac{2\pi}{3}i\right\}$$
$$+\exp\left\{\frac{\pi i}{h}[-(p+2q)y-\sqrt{3}px]+2\pi pi \mp \frac{2\pi}{3}i\right\}$$
$$+\exp\left\{\frac{\pi i}{h}[(p-q)y+\sqrt{3}(p+q)x]-2\pi pi \pm \frac{2\pi}{3}i\right\}$$
$$+\exp\left\{\frac{\pi i}{h}[-(2p+q)y-\sqrt{3}qx]+2\pi qi \mp \frac{2\pi}{3}i\right\}, \tag{49}$$

where the two signs correspond to the following quantum numbers:

$$q = n + 1/3, \quad p = q, q+1, q+2, \ldots, \quad \text{upper sign},$$

$$q = n + 2/3, \quad p = q, q+1, q+2, \ldots, \quad \text{lower sign},$$

$$n = 0,1,2,\ldots . \tag{50}$$

Note that these eigenfunctions are characterized by fractional quantum numbers p and q.

Figure 10 shows the graphics of some of the solutions (47), (48), and (49) for low values of (p,q). Note that these solutions are very similar for the solutions or the Schrödinger equation for a particle in an equilateral triangle.[22]

The above approach cannot be extended straightforwardly to other geometries. The reason for this is a theorem stating that only in the cases of square and triangular boxes the eigenfunctions can be expanded in a finite set of plane waves.[23] On the other hand, if the boundary line does not deviate strongly from a circumference (as, e.g., in higher polygons), we can again construct a finite basis set by making a radial rescaling of the eigenfunctions for a disk with equal area.[24]

IV. NUCLEATION OF SUPERCONDUCTIVITY IN BASIC POLYGONS

Using the developments of the preceding sections we can solve now the LGL equation (34) with the boundary condition (7) for several symmetric structures. An important feature of vector potential gauge approach is its ability to provide accurate description of the order parameter

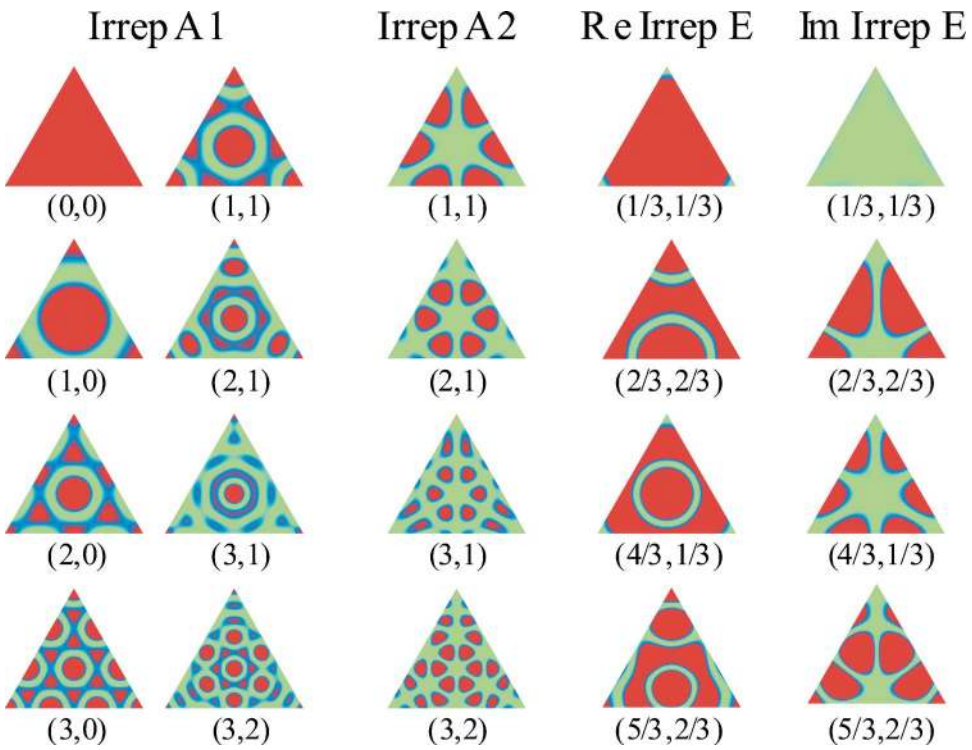

FIG. 10. (Color online) Symmetrized basis functions for an equilateral triangle. The highest density is shown in darker shades and the lowest $|\psi|^2$ values are lighter shades. The numbers in parentheses stand for p and q, respectively.

already for quite limited sizes of the basis sets at moderate applied fields. An accurate calculation of Ψ is often crucial for a correct description of vortex patterns in mesoscopic samples. In this connection we mention that reflections in vertical planes, if they are contained in the symmetry group of the sample, act as time inversion operators, $\sigma_v\Psi=\Psi^*$. Therefore $\Psi^*\Psi$ is invariant under these reflections and the density distribution of the order parameter is described by the full symmetry of the sample.

A. The triangle and square

As shown above it is possible to classify the solutions for a square and a triangle according to the irreducible representations (irreps) of the symmetry groups C_3 and C_4. This classification will include different order parameter patterns, since the solutions are contained in different subclasses characterized by a certain irrep. As can be seen in Figs. 11 and 12 the eigenvalues of the LGL equation belonging to the different irreps will form the complete spectrum of eigenvalues.[25,26] However, *eigenvalues belonging to the same irrep will never cross*. Moreover the lowest eigenvalues form separated bands existing out of an eigenvalue for each irrep, which are crossing in a regular pattern. In this way the H–T phase boundary $T_c(H)$, which is the lowest eigenvalue $E_{\mathrm{LLL}}(H)$, shows an oscillatory cusplike behavior as a function of flux and with every cusp the solution corresponds to a different irrep. The sequence of the $T_c(H)$ oscillations is always A, E_+, B, and E_- in the case of a square, and A, E_+, and E_- in the case of a triangle. The vorticity increases by one when passing a cusp along the H–T phase boundary with increasing field (cf. the Little-Parks experiment) and consequently to the next irrep.

Even as the symmetry of the structure gives rise to a cusplike H–T phase boundary, it still shows a predominantly linear dependence between the magnetic field and the temperature. This is not surprising since a linear H–T phase boundary is the solution for the bulk problem. However, the slope has changed compared to the bulk case, as can be seen in Fig. 13. When comparing the

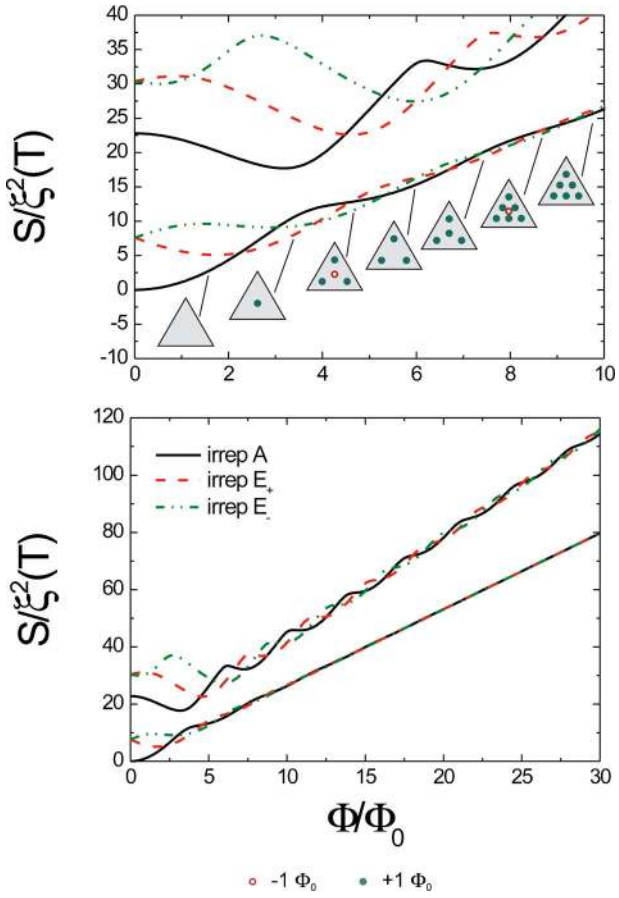

FIG. 11. (Color online) Lower eigenvalues of the LGL equation for the mesoscopic triangle, as a function of the magnetic flux Φ/Φ_0, with superconductor-vacuum boundary conditions. The different lines correspond to the three irreducible representations (irreps) A (full black line), E_+ (dashed red line) and E_- (dashed-dotted-dotted green line). Since the problem has a discrete C_3 symmetry there is a 'repulsion' of the levels, giving a regular pattern of avoided crossing between levels belonging to the same irrep. The flux is defined as $\Phi=\mu_0 HS$, with S the surface of the triangle, $\mu_0 H$ the applied magnetic field and $\Phi_0=h/2e$ the superconducting flux quantum. The lowest sequence of the cusp-like pieces from different irreps forms the lowest eigenvalue $E_{\mathrm{LLL}}(H)$, directly corresponding to the $T_c(H)$ line. For detailed comparison with the experiment see Fig. 19. Along the vertical axis, the critical temperature T_c is linearly decreasing with increasing $S/\xi^2(T)$.

considered shapes with equal surface, it is evident that superconductivity nucleates with decreasing magnetic field H and temperature T, first in the triangle, then the square, the disk[12,28–35] and finally in the bulk material. This can be understood from the results obtained on the nucleation of superconductivity in an infinite wedge[7,8,36–39] where the nucleation field $H_{c3}^{\star}$ increases with reducing angle Γ of the infinite wedge. Consequently we should observe the largest $H_{c3}^{\star}$ for the triangle, since the triangle has the smallest angles in the corners. That is precisely what we observe.

Furthermore, the phase boundary for the square has been calculated by other groups, like Jadallah *et al.*[27] and Schweigert *et al.*[37,40,41] When comparing for instance the positions of the cusps at the phase boundary we see a good agreement between the different calculations at lower fields. However, at higher fields we see a slight deviation between our results and the results of Jadallah *et al.*[27] (see Table I).

Additionally, there is a good agreement between the amplitudes of the oscillations found in our work[26] and Schweigert *et al.*[41] and for certain values of magnetic field and temperature we also find the same vortex patterns. However we also find some large differences in the vortex patterns, specifically vortex-antivortex patterns compared to a giant vortex.

Since the rotational axis in the triangle is of finite order we do not expect the giant vortex state

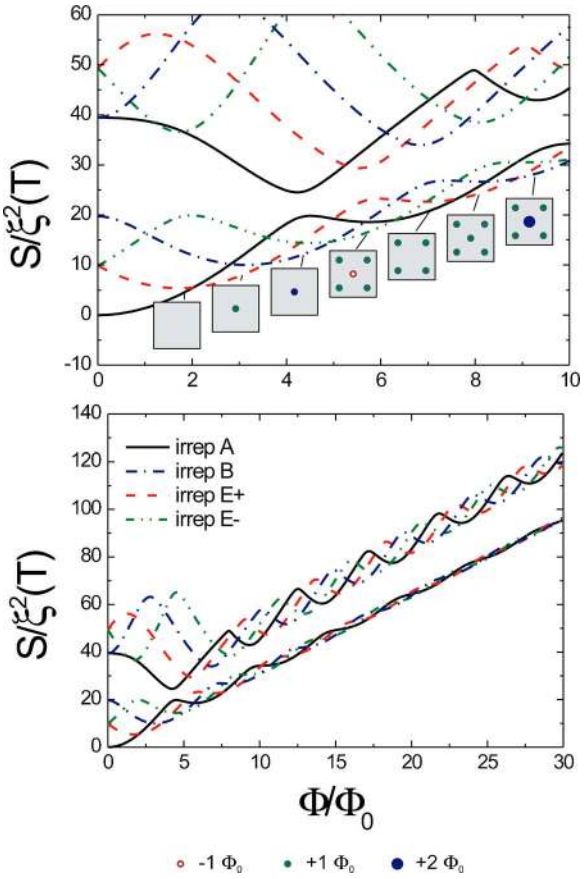

FIG. 12. Lower eigenvalues of the LGL equation for the mesoscopic square, as a function of the magnetic flux Φ/Φ_0, with superconductor-vacuum boundary conditions. The different lines correspond to the four irreducible representations (irreps) A (full black line), B (dashed-dotted line), E_+ (dashed line), and E_- (dashed-dotted-dotted line). Since the problem has a discrete C_4 symmetry there is a 'repulsion' of the levels, giving a regular pattern of avoided crossing between levels belonging to the same irrep. The flux is defined as $\Phi=\mu_0 HS$, with S the surface of the square, $\mu_0 H$ the applied magnetic field and $\Phi_0=h/2e$ the superconducting flux quantum. The lowest sequence of the cusp-like pieces from different irreps forms the lowest eigenvalue $E_{\mathrm{LLL}}(H)$, directly corresponding to the $T_c(H)$ line. For detailed comparison with the experiment see Fig. 20. Along the vertical axis, the critical temperature T_c is linearly decreasing with increasing $S/\xi^2(T)$.

to be always a ground state solution. Actually there are no vortices in the first state ($L=0$), there is one Φ_0 vortex in the cental position in the second state ($L=1$), and there is one $-\Phi_0$ antivortex in the center and three Φ_0 vortices at the diagonal positions in the third state ($L=-1+3=2$). This sequence is periodically repeated when going to higher applied fluxes. For instance, the fourth state ($L=3$) will contain three Φ_0 vortices dispatched along the diagonals of the triangle. Figure 14 shows the distribution of the order parameter in the above states. The total winding number is a sum of the vorticity numbers of the central and diagonal vortices as follows:

$$L = n + 3m,$$

$$n = 0, 1, -1, \tag{51}$$

where $m=0, 1, \ldots$ is the number of vortex triades. The number n in this equation matches the corresponding irrep via Eq. (35).

The seven insets in Fig. 12 show schematically the distribution of vortices in the square, which are clearly different from the giant vortex states.

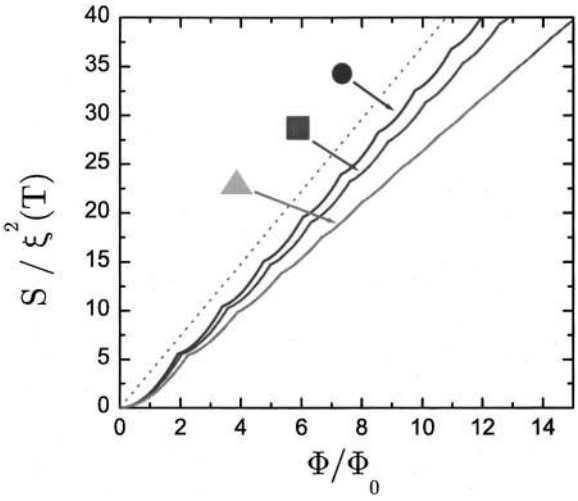

FIG. 13. The calculated *H–T* phase boundary for a disk, square, and triangle. The dotted straight line is the surface critical field for a semi-infinite slab with a straight superconductor/vacuum border $H_{c3}=1.69\,H_{c2}$.

In the case of small L's, vortices can occupy one central and four diagonal positions. In contrast to the diagonal vortices which always enclose a single quantum Φ_0, the central vortex can have different winding numbers in order to conserve the total vorticity of a given state. The contribution of the two kinds of vortices (central+four diagonal) to the total winding number of the states shown in Fig. 12 is given by

$$L = n + 4m,$$

$$n = 0,1,2,-1, \tag{52}$$

where $m=0$, 1. Note that the four numbers in the second equation match the n numbers in the expressions for the basis functions of the corresponding irreps, Eq. (35). This is not surprising since these resemble the eigenfunctions of a 2D rotator with momentum n.

As a result the nature of the central vortex changes, whenever vorticity is changed by one. Thus the central vortex is absent in the first state, it is a Φ_0 vortex in the second state, it is a giant vortex in the third state and it is an *antivortex* (the winding number is negative!) in the fourth state

TABLE I. Calculated cusps positions in $T_c(\Phi)$ for the triangle, the square, and the disk at particular values of the normalized flux Φ/Φ_0. The different calculated values for the square deviate slightly at high winding number L.

$L\rightarrow L+1$ After Ref.	Triangle 25	Square 26	Square 27	Disk 28
$0\rightarrow 1$	2.24	2.04	2.0	1.92
$1\rightarrow 2$	3.88	3.58	3.6	3.39
$2\rightarrow 3$	5.32	4.98	5.0	4.75
$3\rightarrow 4$	6.69	6.32	6.3	6.05
$4\rightarrow 5$	8.01	7.61	7.6	7.31
$5\rightarrow 6$	9.30	8.87	8.9	8.54
$6\rightarrow 7$	10.57	10.12	10.1	9.76
$7\rightarrow 8$	11.82	11.34	11.4	10.96
$8\rightarrow 9$	13.05	12.54	12.7	12.15
$9\rightarrow 10$	14.27	13.74	13.9	13.33

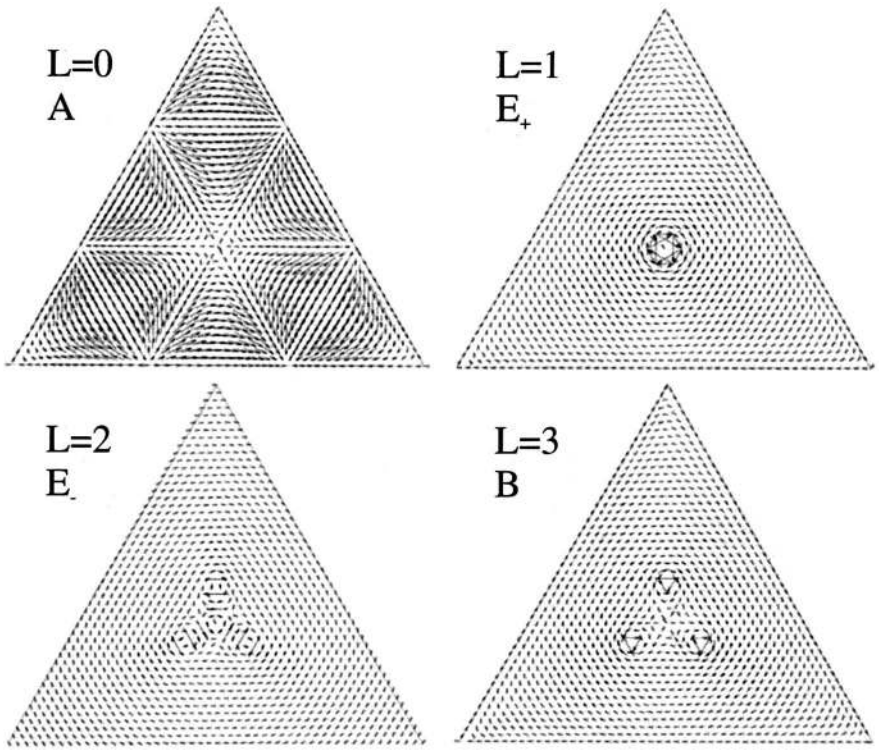

FIG. 14. Gradients of phase of the order parameter at the middle of the lowest four cusps in the $T_c(H)$ phase diagram in Fig. 11. Large arrows rotating clockwise encircle the vortices and those rotating in the anticlockwise direction display the antivortex. The panel for the E_- state, zoomed 16 times, shows the presence of an Φ_0 antivortex in the center.

(see Fig. 12). The sequence of winding numbers of the central vortex $(-1, 0, 1, 2)$ is periodically repeated when going to the right of the phase diagram.

Because the kinetic energy of a vortex is proportional to L^2, the system prefers to split the giant vortex into a sum of smaller vortices[42] if there are no special symmetry restrictions. Another energy based reason is that vortices get attracted to the corners as it was shown for the case of a semi-infinite plane with a wedge.[39] This explains why the four dispatched vortices prefer to stay on the diagonal positions in the ground states. The combination of these two arguments explains why only four numbers mentioned above appear as winding numbers for the central vortex. On the other hand, the formation of antivortices is dictated completely by the discrete symmetry. Indeed, in the state with $L=3$, one cannot distribute three Φ_0 vortices on the square keeping the symmetry. The dilemma is solved by having four diagonal Φ_0 vortices and adding one antivortex in the center.

Figure 15(a) shows the distribution of the order parameter corresponding to the antivortex solution. The central antivortex is separated from vortices on the square diagonals by about 2% of the edge length. The maximal value of the order parameter on the line connecting the antivortex with one vortex does not exceed one-thousandth of its value in the corners of the square. Note that this solution is obtained within the present approach by using a moderate basis set. To reproduce these features by finite grid methods a very large basis set corresponding to at least a 400×400 grid should be involved in the calculations.[43]

At higher values of applied field the additional vortices will continue to occupy the diagonal positions as shown in Fig. 16 for states of symmetry A.

On the whole, the nucleation of superconductivity in squares has similar features with the equilateral triangles. We expect most of these features to be general for higher order regular polygons too since they are based on symmetry grounds. For instance, the avoided crossing

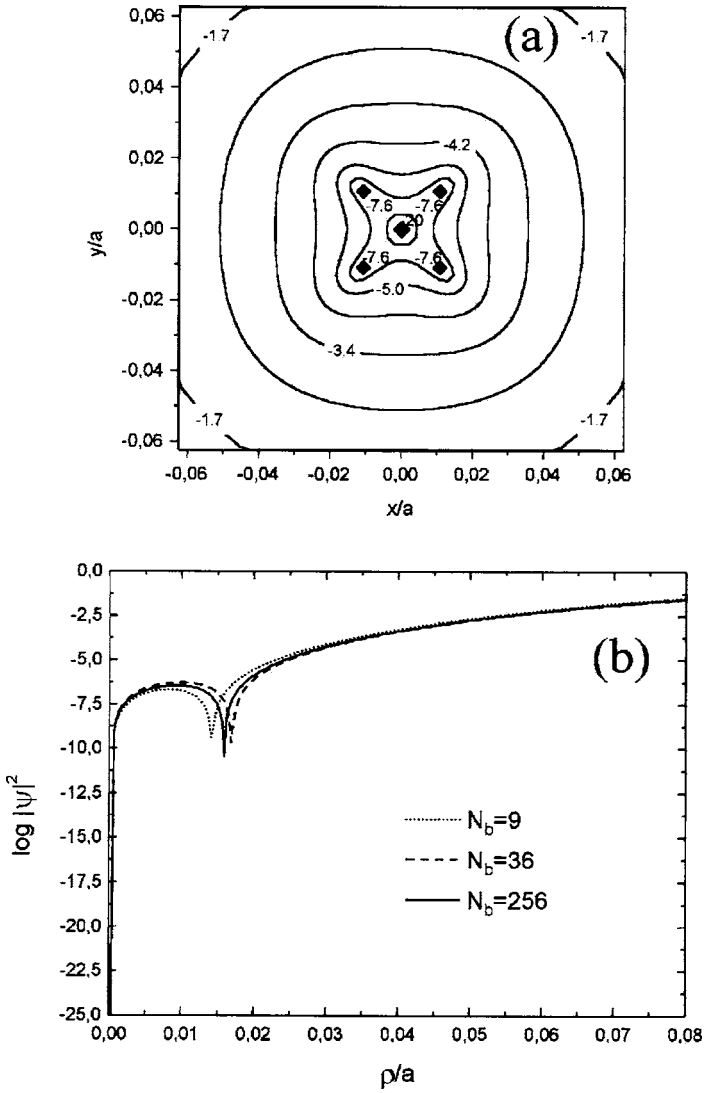

FIG. 15. Order parameter plots corresponding to the ground state of the square in an applied magnetic flux $\Phi=5.5\Phi_0$. The contour plot (a) shows (in logarithmic scale) the vortex pattern in the central region of the square zoomed in eight times after convergence with respect to the basis set size was achieved. The panel (b) displays the cross section in the diagonal direction $\rho=0$ is the center of the square) for different sizes of basis sets used in the calculations.

patterns of levels belonging to the same irrep is a common feature. One can see that it is more pronounced in the triangle (Fig. 11) than in the square (Fig. 12) and will generally diminish with increasing order of the polygon, disappearing completely in the case of disk ($N\rightarrow\infty$). The same for the vortex patterns; they are expected to shrink with increasing N and merge into giant vortex states in the limit of the disk. The asymptotic behavior of the ground state solutions in the limit of high applied field corresponds to the N-fold degenerate ground Landau level, the components of which belong to N different irreps of the corresponding polygon. This becomes infinitely degenerate in the case of disk, containing all different rotational (vorticity) states as components.[11]

B. Experimental phase boundary

To check the theoretical prediction for the lowest Landau level $E_{\mathrm{LLL}}(H)$ for different geometries (triangle, square, disk), superconducting Al samples have been made to measure the $T_c(H)$ line.

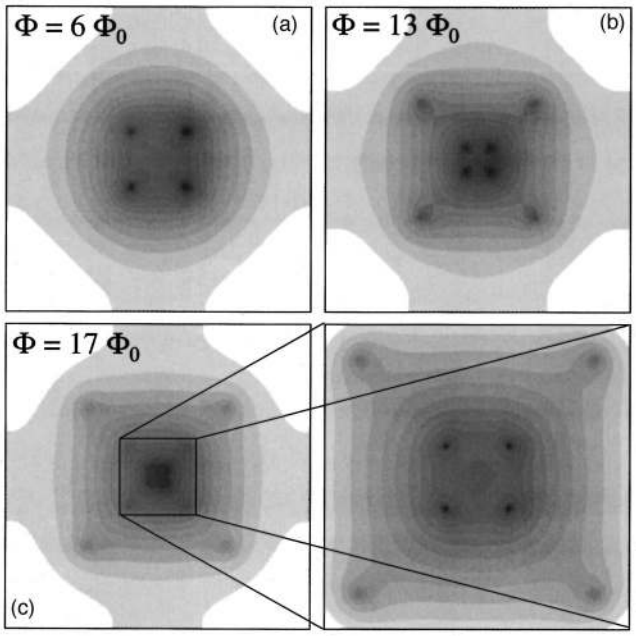

FIG. 16. Three vortex patterns corresponding to the symmetry A of the order parameter and the total vorticity $L=4$ (a), $L=8$ (b), and $L=12$ (c). In all cases the vortices are arranged symmetrically along the diagonals of the square. The panel in the left bottom corner shows the zoomed in central region of the plot c.

1. Sample characteristics

Figure 17 shows AFM and SEM micrographs of the triangle, the square and the disk. Wedge shaped current and voltage leads with an opening angle of $\Gamma=15°$ and with a narrow width of the interface between the structure and the current leads were used in order to minimize their influence on the superconducting properties of the structure.[44,45] The square and the disk were evaporated in the same run. A thickness $\tau=39$ nm was obtained from x-ray and AFM measurements. The radius of the disk, measured with AFM and SEM, was 1 μm. For the square, lateral dimensions of 2×2 μm^2 were obtained. The samples have a coherence length, determined from a coevaporated reference sample, of $\xi(0)=156$ nm and a critical temperature of $T_c=1.32$ and 1.33 K for the square and the disk, respectively. The equilateral triangle has a thickness $\tau=43$ nm, a basis of 2.33 μm. A coherence length of $\xi(0)=130$ nm and critical temperature of $T_c=1.34$ K were found for this sample.

The $T_c(H)$ phase boundary is measured by four-point resistance measurements using a lock-in amplifier. An ac transport current of 0.1 μA is sent through the two current leads (horizontal

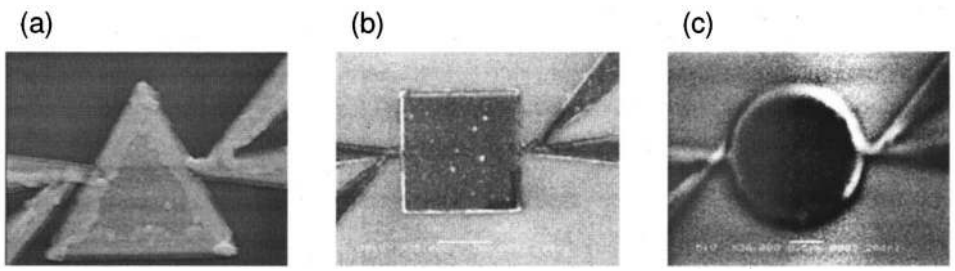

FIG. 17. AFM and SEM micrograph of an Al triangle (a) with basis of 2.33 μm, of a square (b) with a lateral dimension of 2 μm and of a disk (c) with a radius of 1 μm.

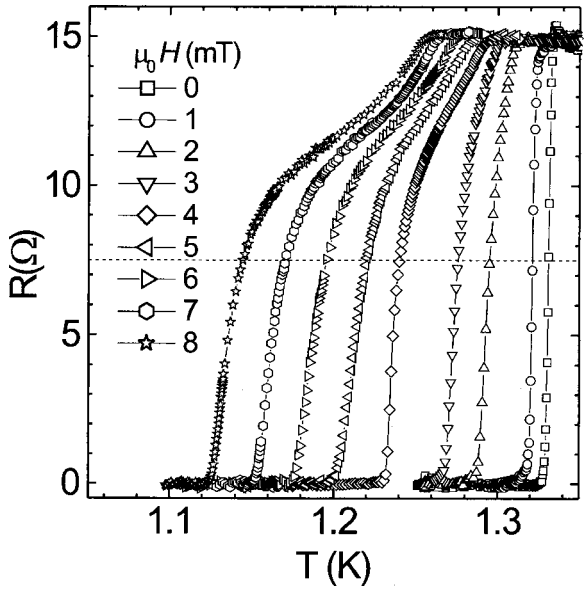

FIG. 18. Resistive transitions $R(T)$ for the triangle in different magnetic fields. From $\mu_0 H=0$ mT (open squares) to 8 mT (open stars). The dashed line shows the resistance criterion used to determine the $T_c(H)$ phase boundary.

contacts in Fig. 28). In order to construct the H–T phase diagram a set of $R(H)$ magnetoresistance curves are measured at various temperatures. The phase line is in a next step extracted from the data using a certain resistance criterion R_c.

2. Triangle

Figure 18 shows the resistive transitions of a mesoscopic triangle with wedge shaped contacts. The $R(T)$ curves are composed of two parts with different slopes. The upper part of this double transition shows a slowly decaying resistance while a steeper drop is seen in the lower part. This effect becomes more pronounced with increasing magnetic field. The appearance of the two distinct parts in the transition curves arises from the different field dependence of the nucleation temperature in the triangle and in the wedge shaped contacts.[45] The upper part of the $R(T)$ curves corresponds to the nucleation in the contacts followed by the nucleation in the triangle for lower temperatures at the lower part. The square and the disk show very similar resistive transitions.

The result of a continuous $T_c(H)$ measurement of a mesoscopic triangle is given in Fig. 19. The $T_c(H)$ phase boundary, measured for the triangle, is shown as open circles in Fig. 19 with the coherence length $\xi(0)=130$ nm determined from a coevaporated reference film and the surface $S=2.36\ \mu\text{m}^2$ found from AFM and SEM investigations. The open squares represent the measured phase boundary with the best fitting parameters, the best value for the coherence length is $\xi(0)=118$ nm and the effective area of the sample $S=2.25\ \mu\text{m}^2$. This leads to a difference of 10% between the measured and the fitted coherence length and a difference of 5% between the measured and the fitted sample areas S. After this small correction an excellent agreement between the experiment and the theory is observed. The amplitude of the oscillations and the position of the cusps are in perfect accordance.

From the AFM and SEM measurements, features that could be attributed to resist at the boundaries of the structures were observed. Since the area written by e-beam lithography was $S=2.25\ \mu\text{m}^2$, we believe that the exact surface of the Al triangle is slightly lower than the measured one ($S=2.36\ \mu\text{m}^2$). Another explanation for the different obtained values of the fitting parameter for the area of the triangle and the measured area could be the error margin on the measured value. A possible reason for the deviation between measured and the fitted coherence length might be the presence of the wedge contacts. The wedge-shaped contacts will probably not change the value of

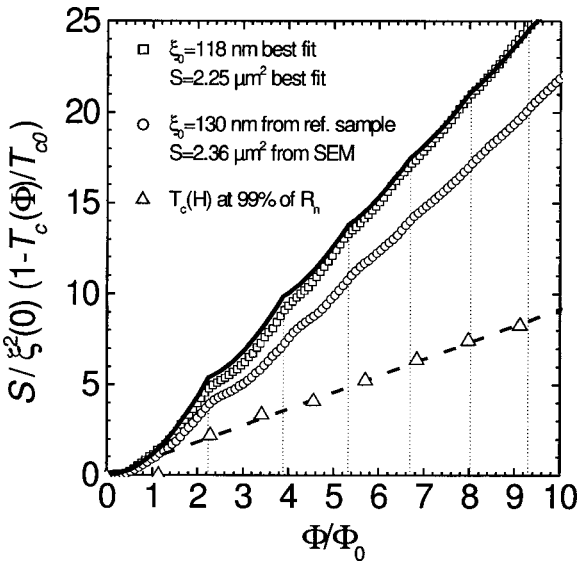

FIG. 19. Experimental $T_c(H)$ phase boundary of an equilateral triangle with wedge-shaped contacts. The open circles represent the data obtained using the measured sample size $S=2.36\ \mu\text{m}^2$ and the coherence length $\xi(0)=130$ nm. The best agreement between the measured and the theoretical phase boundary was found using the parameters $S=2.25\ \mu\text{m}^2$ $\xi(0)=110$ nm, see the open squares in the figure. The full line represents the theoretical curve (Ref. 32). The open triangles are taken from the resistance transition $R(T)$ for a resistance criterion of 99% R_n. The dashed line is the theoretical phase boundary of the wedge-shaped contacts with opening angle $\Gamma=15°$.

the coherence length, but shift the phase boundary of the triangle in the direction of the phase boundary for a wedge with opening angle $\Gamma=15°$. Another possibility for this small discrepancy could be a difference between the coherence length of the coevaporated reference film and the coherence length of the mesoscopic triangle that cannot be measured directly. A potential origin of the discrepancy between the two coherence lengths could be a slight contamination of Al by the resist used in the preparation of the mesoscopic structures, that would decrease the elastic mean free path ℓ_{el} and consequently also ξ. A lower resistance criterion (smaller than the 50% of R_n criterion used) for the determination of the phase boundary, will give a small reduction of the divergence, but cannot remove completely the difference between the two coherence length values. Another reason for this small discrepancy could arise from the not perfectly shaped triangles. Since the opening angle of the corners plays the major role in the determination of the slope of the $T_c(H)$ curve, we could expect that not perfectly sharp corners would decrease the critical field. In our experiment, the measured phase boundaries are shifted to the opposite direction, so that it cannot be attributed to the rounded corners of the triangles.

The open triangles in Fig. 19 show the critical temperature of the triangle for a chosen resistive criterion equal to 99% of the normal state resistance from the $R(T)$ curves. A perfect agreement between the theoretical phase boundary of the contacts and the point on the $R(T)$ curve where the resistance starts to drop is observed. The double resistance transition observed in the measurements (see Fig. 18) is therefore due to two different superconducting/normal transitions. From this observation, it is clear that the resistance criterion for the determination of the phase boundary of the structure must be chosen in the low resistance region of the $R(T)$ transition. If the resistance chosen for this criterion is too high, the nonlocal effect of the contacts on the triangle will be probed.

3. Square

The experimental phase boundary of a square is displayed in Fig. 20 and is compared with the theoretical calculations. While previous measurements[2,46] showed a strongly oscillating $T_c(H)$ dependence superimposed with a pronounced quadratic background, our results are in very good

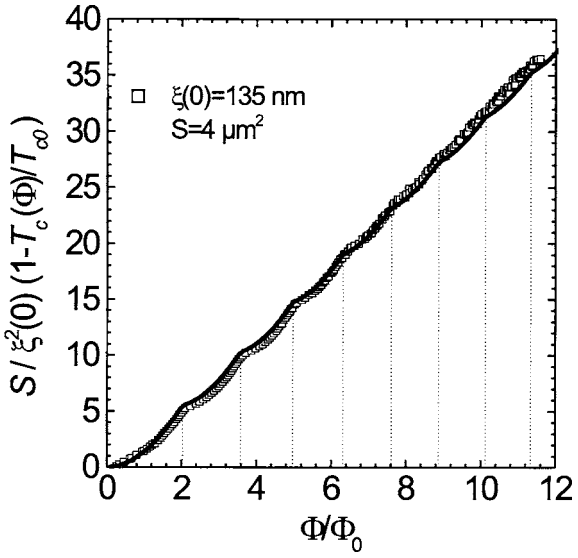

FIG. 20. Experimental $T_c(H)$ phase boundary of a square. The open squares represent the measured value using the measured sample size $S=4\ \mu\text{m}^2$ and the coherence length $\xi(0)=135$ nm. The full line is the theoretical curve $E_{\text{LLL}}(H)$.[26]

agreement with the theoretical predictions. Only a smaller coherence length $\xi(0)=135$ nm was used. The second parameter S used to compare the experimental and the theoretical data was found to be in the error margin of the determined area from SEM and AFM measurements. The main difference between the presented experimental phase boundary and previous reports is the shape and the size of the current and voltage contacts that can be extremely invasive in mesoscopic superconductors.

4. Disk

The $T_c(H)$ phase boundary of the disk is shown in Fig. 21 using a resistance criterion of

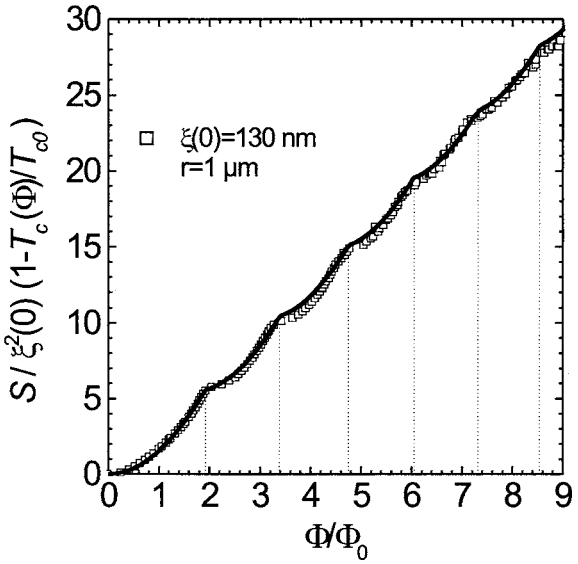

FIG. 21. Experimental $T_c(H)$ phase boundary of a disk determined for a resistance criterion of $2/3\,R_n$. The open squares represent the measured value using the radius $r=1\ \mu$m and the coherence length $\xi(0)=130$ nm. The full line is the theoretical curve $E_{\text{LLL}}(H)$.

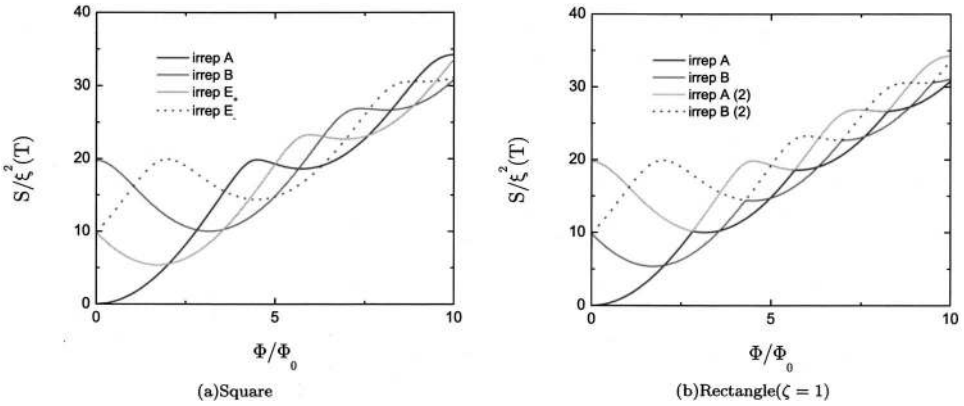

FIG. 22. In the case of the square [panel (a)] the lowest Landau level is constructed by the four lowest eigenvalues, corresponding to different irreps. However, the lowest Landau level $E_{\mathrm{LLL}}(H)$ in the rectangle with aspect ratio one [panel (b)] is obtained from just the lowest two eigenvalues, and the same spectrum of eigenvalues is formed with the two lowest pairs of eigenvalues. Deviations from aspect ratio one for the rectangle will lead to a gap between these two pairs of eigenvalues.

$2/3\,R_n$. Already in 1965, Saint-James calculated the phase boundary of a singly connected cylinder[9] with the gauge chosen as $\vec{A}=(\mu_0 Hr/2)\vec{e}_\phi$. With this particular choice, the superconducting boundary condition is imposed only on the gradient of the order parameter $|\Psi|$ along the radial axis. Since under these conditions $|\Psi|$ has no z-dependence, the phase boundary of a disk or an infinitely long cylinder will be the same. The solution of the linearized GL equation for a disk is a Kummer function of the first kind.[28,29] The nucleation temperature at a fixed magnetic field value can be found by taking the vorticity L that minimizes the eigenvalue giving rise to a cusplike phase boundary as shown by the full line in Fig. 21.

In order to fit the theoretical curve, the measured value of the radius $r=1$ μm and a slightly different coherence length of 130 nm, instead of the value of 154 nm determined from the reference sample, were used. After this small correction a good agreement is found between the theoretical and the experimental phase boundary for the position of the cusps. However, as in the measurements of Buisson *et al.*,[47] where a substantially larger disk was measured, the amplitude of the oscillation in the experimental curve is stronger than for the theoretical predictions. In our experiment, an excellent agreement between the theory and the experiment was found (see Fig. 21) by using a resistance criterion of $2/3\,R_n$. The positions of the cusps as well as the amplitude of the oscillations in the experimental curve match the theoretical phase boundary.

C. From square to rectangle

When crossing over from a square ($\zeta=1$) to a rectangle, we should go from a fourfold to a twofold rotational symmetry. The lowest Landau level in a superconducting square follows a cusplike profile corresponding to successive crossings of the solutions corresponding to four different representations. This is reproduced in the rectangle with aspect ratio one by a pair of crossing irreducible representations (irreps). However to obtain the full spectrum of eigenvalues formed by the four lowest crossing solutions in a square, two pairs of crossing irreps are needed, not only the lowest solutions but also the first excited ones of the A and B symmetry (see Fig. 22).[48] Departure from aspect ratio one leads to a splitting between the lowest and first excited solutions. Small deviations from the square have no noticeable effect on the lowest Landau level. All aspect ratios close to one have a lowest Landau level showing an oscillatory behavior with a predominantly linear background dependence on the field.

At a field of 5 up to 6.3 Φ/Φ_0 we find that the lowest Landau level corresponds to a solution with vorticity three. Although the energy levels and vorticity of all rectangles with an aspect ratio very close to one are the same, the vortex pattern can nevertheless be very different (Fig. 23). In

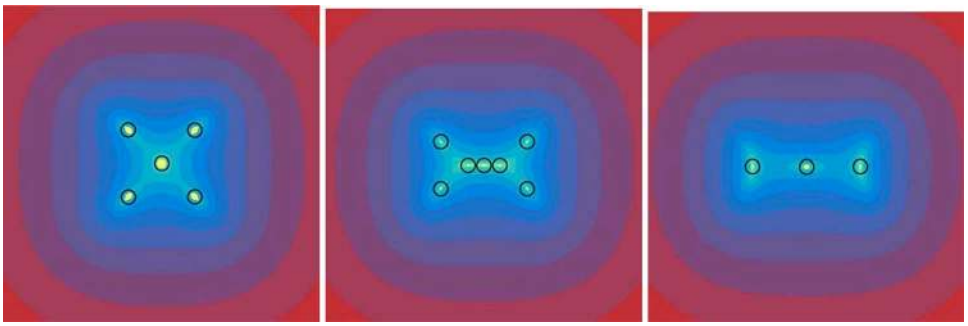

FIG. 23. (Color online) The figures show the density of the order parameter $|\psi|^2$ of the central $(a/10)\times(b/10)$ region in the rectangle in a log scale, where a is the long side and b is the short side. The highest density is shown in darker shades and the lowest $|\psi|^2$ values are in lighter shades, indicating the position of vortices and antivortices. Every shade corresponds to roughly half an order of magnitude. At a field of 5.5 Φ/Φ_0 the rectangles with, respectively, aspect ratio 1, 1.01, and 1.02 have very different vortex patterns. For aspect ratio one we observe the known configuration with one antivortex in the center and four vortices on the diagonals. However, at aspect ratio 1.01 we see four vortices on the diagonals, one in the center and two antivortices next to the central vortex. Finally at aspect ratio 1.02 we find that there are three vortices positioned on the long axis of the rectangle.

a *square* vorticity three is formed by *four vortices on the diagonals and one antivortex in the center*. At an aspect ratio 1.02 vorticity three already corresponds to *three vortices on a row* along the longest axis. However when we consider an aspect ratio 1.01, which lies between these two values, the pattern is more complex. The vortex pattern is now built up from four vortices on the diagonals, one vortex in the center and two antivortices located on the left and right from the central vortex along the long axis. This suggests the following evolution from aspect ratio 1 to aspect ratio 1.02. By varying the aspect ratio from one the antivortex in the center splits into two antivortices plus one vortex in the center. These antivortices move away from the center along the long axis, where each antivortex merges with the pair of vortices, respectively, at the left and right of the antivortex, leaving as a result three vortices on the longest axis. We must point out that the vortex pattern observed at aspect ratio 1.01 with a central vortex and two neighboring antivortices is in itself embedded into a region where the order parameter is already suppressed by orders of magnitude, which implies that we can also consider this structure as one elongated antivortex with a nontrivial $(-1+1-1)$ core structure.

1. Larger aspect ratios

It is surprising to see that the H–T phase boundary [Fig. 24(a)] remains almost the same for the aspect ratio between 1 and 1.333. However, the amplitude of the oscillations within the same irrep is reduced without substantial change in the lowest Landau level. Only when the aspect ratio becomes two or larger, a noticeable shift in the lowest Landau level is seen. Except for the first cusp the lowest Landau level still shows an oscillatory behavior on top of a linear dependence on the field, though with a reduced slope. At an aspect ratio of four we can hardly observe the crossing of the different irreps as they almost completely merge together, only the first cusp remains clearly visible. For fields higher than the first crossing of solutions, the field dependence becomes again linear. The same pattern persists for even higher aspect ratios. However, the field, at which the solutions for the first time cross, increases with the aspect ratio (Fig. 25). This crossing of the two irreps corresponds to the appearance of the first vortex in the rectangle, because the irrep B describes solutions that have a vortex in the center, while the irrep A solutions are without a vortex in the center. As a consequence every crossing of the solutions corresponding to the two irreps, will change the vorticity by one. The H–T phase boundaries for the different aspect ratios not only show the same behavior, they additionally can be scaled on one *universal* curve, apart from the oscillations [Fig. 24(b)]. The scaling is performed by dividing $S/\xi^2(T)$ and Φ/Φ_0 by the aspect ratio ζ,

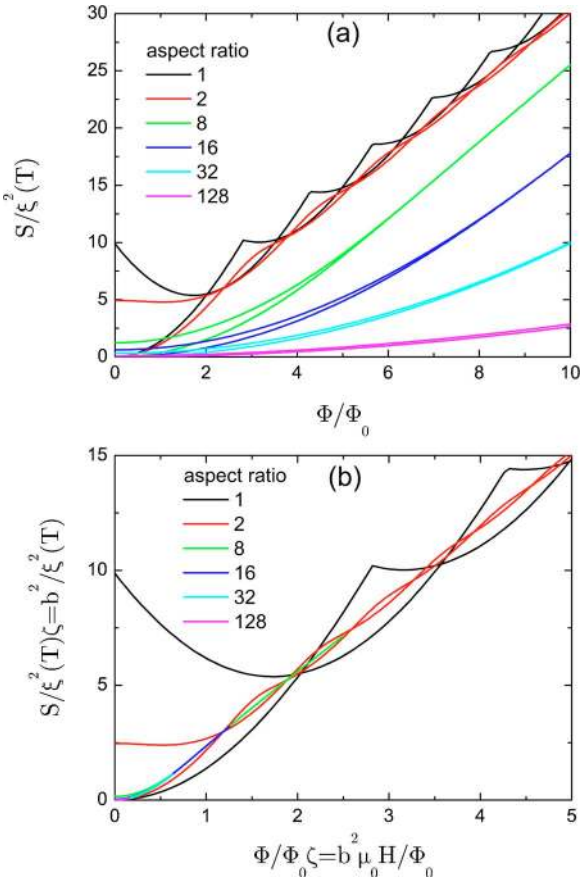

FIG. 24. (Color online) (a) Calculated superconducting H–T phase boundary for rectangles with different aspect ratios. The superconducting phase is located above (lower T) and the normal phase below the H–T phase boundary. For every aspect ratio the lowest two eigenvalues of the LGL equation for the mesoscopic rectangles with superconductor-vacuum boundary conditions as a function of magnetic flux Φ/Φ_0 are shown, with the lowest eigenvalue $E_{\mathrm{LLL}}(H)$ corresponding to the phase boundary. The different shades correspond to different aspect ratios, as indicated in the figure, however with the same surface S. The lowest graph at zero field for the same shade is the solution for irrep A and the highest graph is the solution for irrep B. The flux is defined as $\Phi=\mu_0 HS$ with S the surface of the rectangle, $\mu_0 H$ the applied magnetic field. (b) Different H–T phase boundaries show fundamentally the same behavior in a different field and temperature range, by scaling the different curves with the aspect ratio ζ onto the same universal curve, apart from the oscillations.

$$\frac{ab}{\xi^2(T)\zeta}=\frac{b^2}{\xi^2(T)},\quad \frac{\Phi}{\Phi_0\zeta}=\frac{ab\mu_0 H}{\Phi_0\zeta}=\frac{b^2\mu_0 H}{\Phi_0}. \tag{53}$$

Therefore we can conclude that the length b of the shortest side of the rectangle controls to a large part the behavior of the superconducting mesoscopic rectangle, such as the entry of the first vortex and the slope of the phase boundaries.

Since the curves can be scaled on a universal curve neglecting the cusps, it is also possible to describe the H–T phase boundary with a single function with the same dependence on the aspect ratio as the scaling,

$$\frac{S}{\xi^2(T)}=\frac{3}{\zeta}\left(\frac{\Phi}{\Phi_0}\right)^2\quad\left(\frac{\Phi}{\Phi_0}<0.535\zeta\right), \tag{54}$$

$$\frac{S}{\xi^2(T)}=6\left(\frac{\Phi}{\Phi_0}\right)-3(0.535)^2\zeta\quad\left(\frac{\Phi}{\Phi_0}\geqslant 0.535\zeta\right). \tag{55}$$

However, this fit only works well at aspect ratio $\zeta\geqslant 4$ where the cusps are negligible.

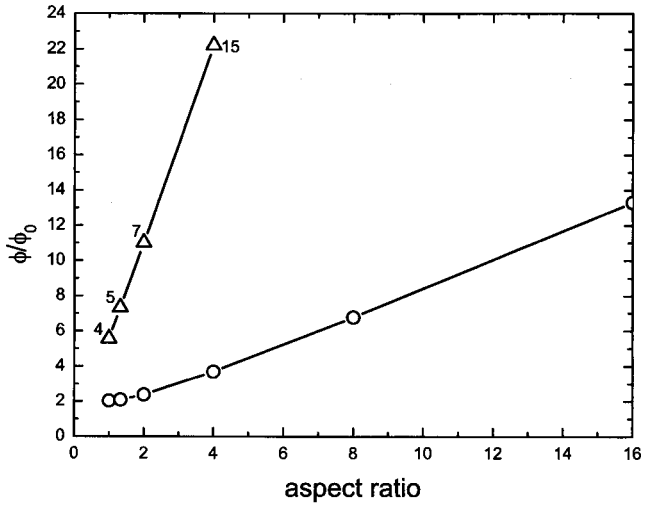

FIG. 25. The circles show the flux at which the first vortex enters the rectangle. The open triangles are the first points on the T_c–H phase boundary where vortices are located on the bisectors for the different aspect ratios. The numbers next to the squares indicate the corresponding number of vortices present in the rectangle at these fields.

In the case of aspect ratio 1.333 the vortices are situated in the central region on the longest axis of the rectangle. However, when the vorticity equals four, the vortices are sitting very close together. As a consequence the vortices move away from the axis and instead are placed on the *bisectors*, which go from the corners to the long axis of the rectangle (see also Fig. 27). The subsequent vortices appear again on the longest axis until the vorticity becomes 12. At this point another four vortices move away from the axis towards the corners along the bisectors. This of course is in contrast to the square where all the vortices are always on the diagonals at the H–T phase boundary in the considered field range.

The preference for positioning the vortices on the bisectors originates from the observed Meissner currents (Fig. 26) which make a hard bend there up to the longest axis (very weak screening), therefore the kinetic energy of the supercurrents is lower when a vortex is present on these bisectors compared to when a vortex is positioned away from the bisectors and from the

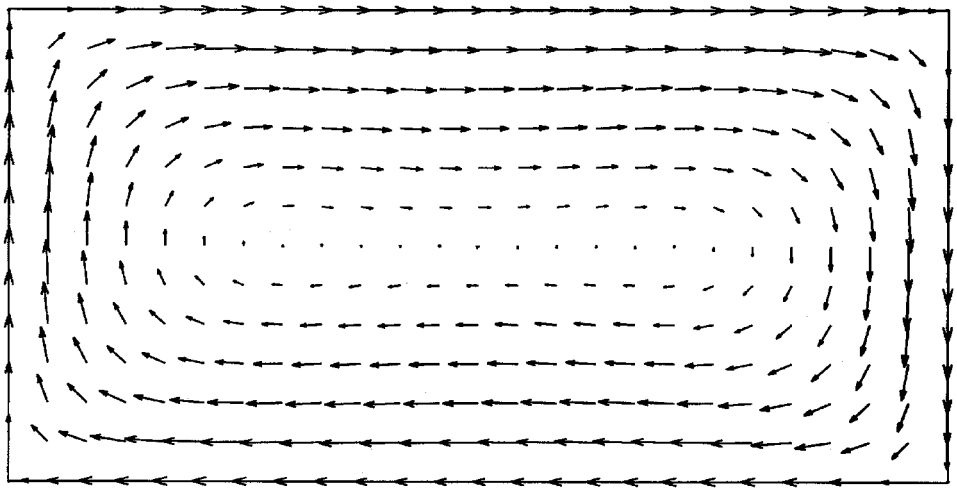

FIG. 26. The graph shows the supercurrents in arbitrary units in a rectangle with aspect ratio two just before the entrance of the first vortex at a magnetic field giving rise to magnetic flux of $\Phi=2.2\Phi_0$.

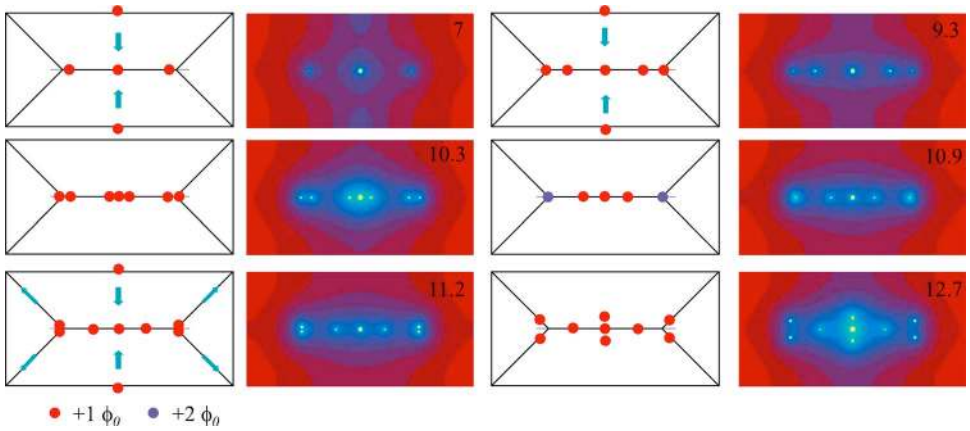

FIG. 27. (Color online) The figures show the evolution of the vortex pattern in the rectangle with aspect ratio two while following a single solution corresponding to irrep B with increasing field. The same shade conventions as in Fig. 23 were used. The numbers indicate the flux in the rectangle in units of the flux quantum Φ_0. The black lines are constructed by dividing the long axis with length a in three regions. Both outer regions have a length of $b/2$. If we would remove the central region, a square would remain with the black lines forming its diagonals.

central region of the longest axis. A similar pattern of Meissner currents leads to a discontinuity along the bisectors in the problem of the entry of flux lines in a rectangle away from the H–T phase boundary observed by magneto-optical techniques.[49–51]

The same scheme repeats itself for aspect ratio two. However we must wait until there are seven vortices in the rectangle before four vortices start to be located on the bisectors. For the aspect ratio four it takes 15 vortices to initiate the vortex redistribution from the axis to the bisectors. So it is clear that with growing aspect ratio the field at which the vortices start to take positions on the bisectors increases. From Fig. 25 we can see that the lowest field at which vortices appear first at the bisectors increases linearly with the aspect ratio for at least the lowest aspect ratios. For aspect ratios beyond four we cannot go high enough in field with a basis set of 1764 basis functions to see vortices on the bisectors. For the largest aspect ratios even the entrance of the first vortex in the rectangle is beyond the field range accessible for a limited number of basis functions in the set.

In summary it has been shown that the vortex pattern in a rectangle is composed of a central row of vortices along the longest axis and the vortices that are situated on the bisectors. These bisectors span the left and right $b/2$ region, where b is the short side of the rectangle. The vortices forming a row parallel to the longest axis only move into these two outer regions when they are ready to reposition themselves onto the bisectors, as shown in Fig. 27. When following the same irrep with increasing field (Fig. 27), we can observe the vortices enter in pairs through the centers of the long edges. When more vortices accumulate on the central line, migration starts to the outer $b/2$ regions. In this region on the longest axis two pairs of vortices will merge at the two points where the bisectors cross and form two giant vortices with vorticity two. These giant vortices split again into separate vortices which move along the bisectors now.

2. Lines

When increasing the aspect ratio to large values, the rectangle eventually resembles a line. The H–T phase boundary for a line with a width smaller than the coherence length $\xi(T)$ in a perpendicular magnetic field is well known for the London limit since it coincides with the problem of a thin (thickness $\ll\xi(T)$) superconducting plane in a parallel magnetic field.[1,52] We have

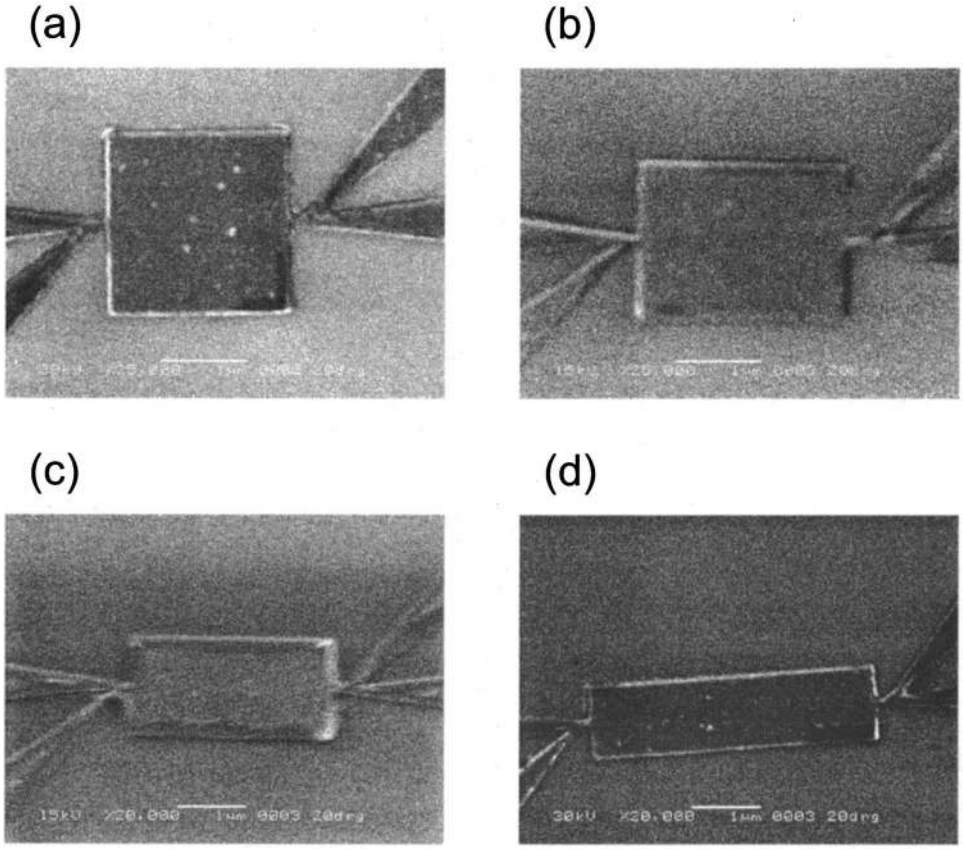

FIG. 28. SEM micrograph (a) of an Al square with lateral dimensions 2×2 μm^2 ($\zeta=1$) and of a rectangle with lateral dimensions of (b) 1.73×2.31 μm^2 ($\zeta=4/3$), (c) 1.41×2.83 μm^2 ($\zeta=2$), and (d) 1×4 μm^2 ($\zeta=4$).

$$\frac{1}{\xi^2(T)}=\frac{\pi^2w^2\mu_0^2H^2}{3\Phi_0^2}. \tag{56}$$

We can get an approximation for the rectangle with large aspect ratio when we substitute the width w^2 with $b^2=ab/\zeta$ where ζ is the aspect ratio, a is the long side, and b is the short side of the rectangle,

$$\frac{ab}{\xi^2(T)}=\frac{\mu_0^2\pi^2}{3\zeta}\left(\frac{\Phi}{\Phi_0}\right)^2. \tag{57}$$

This solution, which is obtained by minimizing the GL free energy in the London limit, is only valid when $|\Psi|$ is approximately spatially constant. Consequently the valid field region will increase with aspect ratio, since the field of the first entrance of a vortex increases with increasing aspect ratio. For instance, we determined that within the shown field region this approximation already coincides perfectly with our calculations for a rectangle with aspect ratio 64.

D. Experimental phase boundary

To investigate experimentally the crossover square-rectangle, four rectangles with different aspect ratio ($\zeta=1$, $4/3$, 2, and 4) were studied. They were all evaporated in the same run. The four structures have the same area of $S=4$ μm^2. A SEM micrograph of the studied samples is shown in Fig. 28. The rectangles with aspect ratio $\zeta=1$, $4/3$, 2, and 4 have dimensions of 2×2 μm^2,

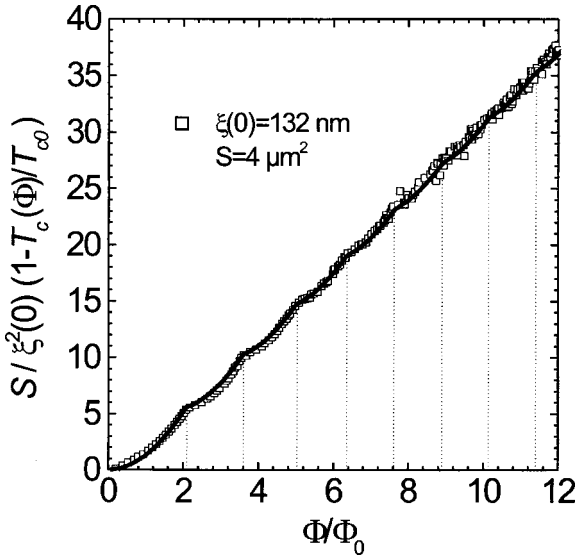

FIG. 29. Experimental $T_c(H)$ phase boundary of a rectangle with $\zeta=4/3$. The open squares represent the measured value using the measured sample size $S=4\ \mu\text{m}^2$ and the coherence length $\xi(0)=132$ nm. The full line is the theoretical curve $E_{\text{LLL}}(H)$.

$1.73\times2.31\ \mu\text{m}^2$, $1.41\times2.83\ \mu\text{m}^2$, and $1\times4\ \mu\text{m}^2$. The thickness τ is 39 nm and the coherence length of the coevaporated reference sample is 156 nm.

The experimental $T_c(H)$ curve of the different rectangles is presented in Figs. 29, 30, and 31. The critical temperature of the rectangles with $\zeta=4/3$ (Fig. 29) and 2 (Fig. 30) shows small oscillations superimposed with a linear dependence of the magnetic field. They have an almost identical phase boundary as the square (see Fig. 20). Only very small changes in the position of the cusps are observed. The magnetic field value where the vorticity changes from L to $L+1$ is slightly delayed when changing the value of ζ from one. No significant change in the slope and the amplitude of the oscillations could be observed.

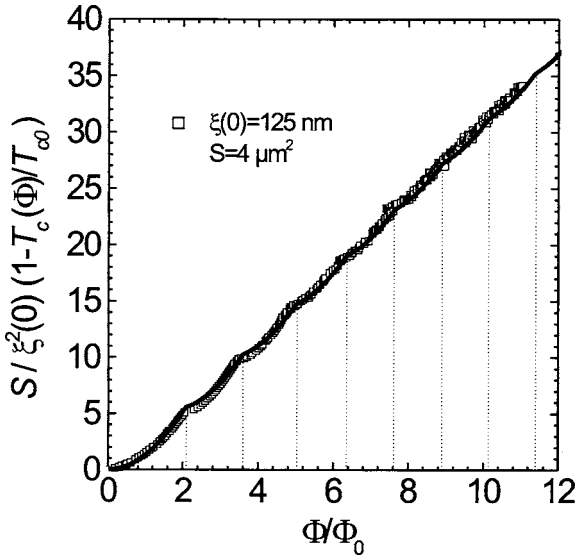

FIG. 30. Experimental $T_c(H)$ phase boundary of a rectangle with $\zeta=2$. The open squares represent the measured value using the measured sample size $S=4\ \mu\text{m}^2$ and the coherence length $\xi(0)=125$ nm. The full line is the theoretical curve $E_{\text{LLL}}(H)$.

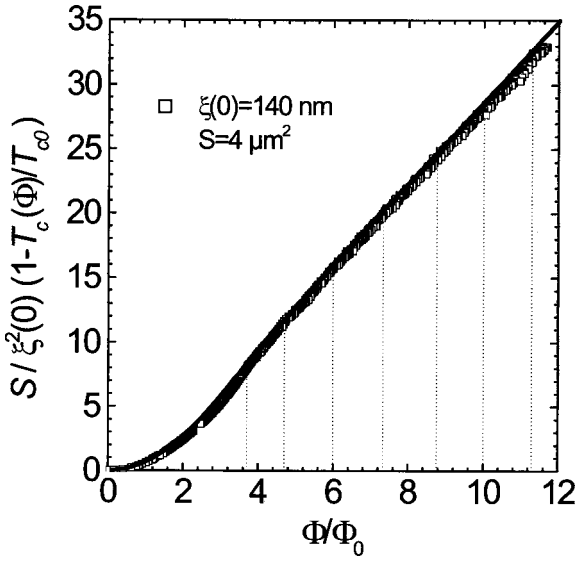

FIG. 31. Experimental $T_c(H)$ phase boundary of a rectangle with $\zeta=4$. The open squares represent the measured value using the measured sample size $S=4$ μm^2 and the coherence length $\xi(0)=140$ nm for a resistance criterion of 40% of R_n. The full line is the theoretical curve $E_{\mathrm{LLL}}(H)$.

A very good agreement between the experimental and the theoretical curves, as well as for the position of the cusp as for the amplitude of the oscillations, is obtained for these two rectangles. Even a large deformation of the square ($\zeta=2$) gives only minor changes in the phase boundary.

For a rectangle with aspect ratio $\zeta=4$, the phase boundary (Fig. 31) is strongly transformed compared to the case of the square. The oscillations are hardly seen and the position of the first vortex entry is delayed to $\Phi/\Phi_0\cong 3.7$ (left dotted line in Fig. 31) instead of the value of $\Phi/\Phi_0 \cong 2$ found for a square. A good agreement between the experimental and the theoretical curves is obtained for a resistance criterion of 40% of R_n.

V. SUPERCONDUCTING RINGS

A. Theoretical formalism

Bruyndoncx *et al.*[53] solved the linear GL equation for a loop of finite width by neglecting the induced magnetic fields. These two assumptions are valid near the phase boundary where $\Psi \to 0$. Using polar coordinates, with the gauge chosen as $\vec{A}=(\mu_0 Hr/2)\vec{e}_\phi$ so that the vector potential has no radial component, the boundary conditions reduce to the simple case of the Neumann boundary conditions,

$$\left.\frac{\partial|\Psi(r)|}{\partial r}\right|_{r=r_o,r=r_i}=0. \tag{58}$$

The solution for Ψ in cylindrical coordinates takes the following form:[11,28,29,54,55]

$$\Psi(\Phi,\varphi)=e^{-iL\varphi}\left(\frac{\Phi}{\Phi_0}\right)^{L/2}\exp\left(-\frac{\Phi}{2\Phi_0}\right)\times\left(c_1 M\left(-n,L+1,\frac{\Phi}{\Phi_0}\right)+c_2 U\left(-n,L+1,\frac{\Phi}{\Phi_0}\right)\right), \tag{59}$$

where the number n determines the energy eigenvalue and M and U are Kummer functions of the first and second kind, respectively.

The eigenenergies of Eq. (4) are

$$|-\alpha| = \hbar \frac{2e\mu_0 H}{m^\star}\left(n+\frac{1}{2}\right) = \hbar\omega\left(n+\frac{1}{2}\right). \tag{60}$$

It is worth emphasizing that the parameter n depends on L but is not necessarily an integer number. This can be rewritten as

$$\frac{r_o^2}{\xi^2(T_c)} = \frac{r_o^2}{\xi^2(0)}\left(1-\frac{T_c(H)}{T_{c0}}\right) = 4\left(n+\frac{1}{2}\right)\frac{\Phi}{\Phi_0} = \epsilon(H_{c3}^*)\frac{\Phi}{\Phi_0}. \tag{61}$$

The Landau levels in a bulk superconductor are recovered by substituting $n=0,1,2,\ldots$ in Eqs. (60) and (61), meaning that the lowest level $n=0$ corresponds to the upper critical field. It is important to note that the lowest Landau level ($n=0$) for a bulk superconductor is degenerate in the phase winding number L, and therefore the eigenfunction can be expanded as $\Psi=\Sigma c_L \Psi_L$.

Using $\mathrm{d}M(a,c,y)/\mathrm{d}y=(a/c)M(a+1,c+1,y)$ and $\mathrm{d}U(a,c,y)/\mathrm{d}y=-aU(a+1,c+1,y)$ for the derivatives of the first and second type of Kummer functions, respectively,[16] and inserting Eq. (59) into Eq. (58) gives

$$\begin{aligned} c_1\left[\left(L-\frac{\Phi}{\Phi_0}\right)M(-n,L+1,\Phi/\Phi_0) - \frac{2n}{L+1}\frac{\Phi}{\Phi_0}M(-n+1,L+2,\Phi/\Phi_0)\right] \\ + c_2\left[\left(L-\frac{\Phi}{\Phi_0}\right)U(-n,L+1,\Phi/\Phi_0) + 2n\frac{\Phi}{\Phi_0}U(-n+1,L+2,\Phi/\Phi_0)\right]\Bigg|_b = 0, \end{aligned} \tag{62}$$

which must be solved numerically for each integer value of L, resulting in a set of values $n(L,\Phi)$, with $\Phi=\mu_0 H\pi r_o^2$.

For a disk geometry,[9,11,47] we must take $c_2=0$ in Eqs. (59) and (62) in order to avoid the divergency of $U(a,c,y\to 0)=\infty$ at the origin. Following the lowest Landau level at each value Φ, one ends up with a cusplike $T_c(H)$ phase boundary,[9] which is composed of values $n<0$ in Eq. (60), thus leading to $H_{c3}^*(T)>H_{c2}(T)$. A similar calculation was performed for a single circular microhole in a plane film by Bezryadin *et al.*,[54,55] where $c_1=0$ in Eqs. (59) and (62), since $M(a,c,y\to\infty)=\infty$. Here as well, the lowest Landau level consists of solutions with $n<0$. At each cusp in $T_c(\Phi)$, the system makes a transition $L\leftrightarrow L+1$, i.e., a vortex penetrates or is expelled from the sample.

The loops of finite width discussed in this section have two superconducting/vacuum interfaces, one at the outer radius r_o, and one at the inner radius r_i. Consequently, the boundary condition [Eq. (62)] must be fulfilled at both r_o and r_i. As a result, we have a system of two equations and two variables n and c_2 ($c_1=1$ is chosen), which were solved for different values of $x=r_i/r_o$. Note that in this case n is a positive or a negative number, just found from these two equations, it is not necessarily a positive integer number.

B. Sample properties

A SEM micrograph of the different studied samples prepared with *e*-beam lithography is given in Fig. 32. All the structures consist of disks with external radii of $r_o=1$ μm. The radii of the holes, determined from SEM micrograph, were $r_i=0$ μm (a), $r_i=0.1$ μm (b), $r_i=0.3$ μm (c), $r_i=0.5$ μm (d), and $r_i=0.7$ μm (e). All the samples were evaporated in the same run, except for the thinnest loop. A different evaporation will only slightly alter the superconducting properties like the coherence length and the critical temperature. Wedge shaped contacts with opening angle $\Gamma=15°$ are used in order to minimize the influence of the contacts on the superconducting properties of the structures.[44,45] The coherence length determined from a macroscopic coevaporated sample was found to be $\xi(0)=156$ nm for the disk and the three loops with a small opening. The thickness was $\tau=39$ nm. For the sample presented in Fig. 32(e), a coherence length of $\xi(0)=120$ nm was determined in the same way as for the other structures. A thickness of $\tau=54$ nm was found from low angle x-ray diffraction on a coevaporated film and from AFM for the loop with $r_i=0.7$ μm.

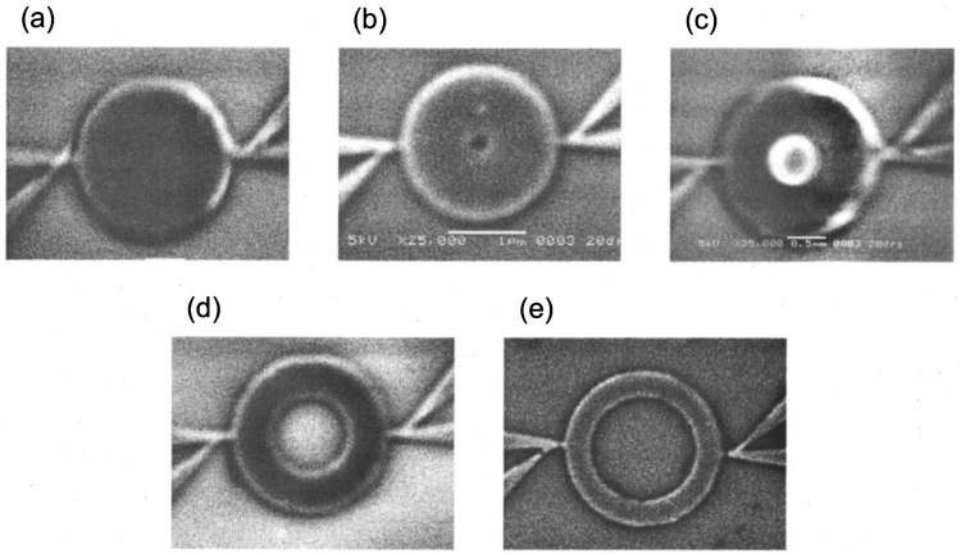

FIG. 32. SEM micrograph of (a) an Al disk with outer radius $r_o=1$ μm and of a loop with outer radius $r_o=1$ μm and inner radius (b) $r_i=0.1$ μm, (c) $r_i=0.3$ μm, (d) $r_i=0.5$ μm, and (e) $r_i=0.7$ μm.

C. Resistance transitions

The superconducting/normal resistance transitions for the disk and the rings with an inner to outer radius ratio $x=r_i/r_o=0.7$ are shown in Fig. 33. The five different samples have a very similar temperature dependence of the resistance at different magnetic field as the samples with wedge shaped contacts with opening angle $\Gamma=15°$ presented above. They are characterized by a slowly decreasing resistance at high temperatures arising from the nucleation of superconductivity in the wedge contacts, followed by a sharp drop of the resistance once superconductivity nucleates in the ring.[56] The samples with $x=0.3$, $x=0.5$, and $x=0.7$ show a different behavior at low magnetic

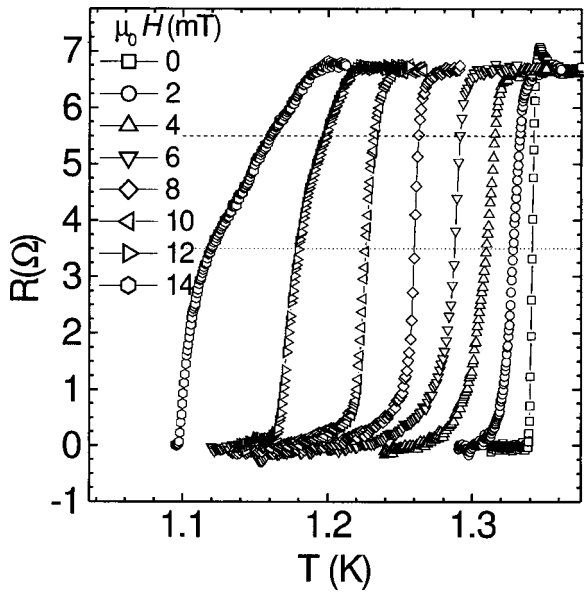

FIG. 33. Resistive transitions $R(T)$ for a loop with inner to outer radius ratio $x=0.7$ in different magnetic fields. The dashed and dotted lines show the resistance criteria used to determine the $T_c(H)$ phase boundary.

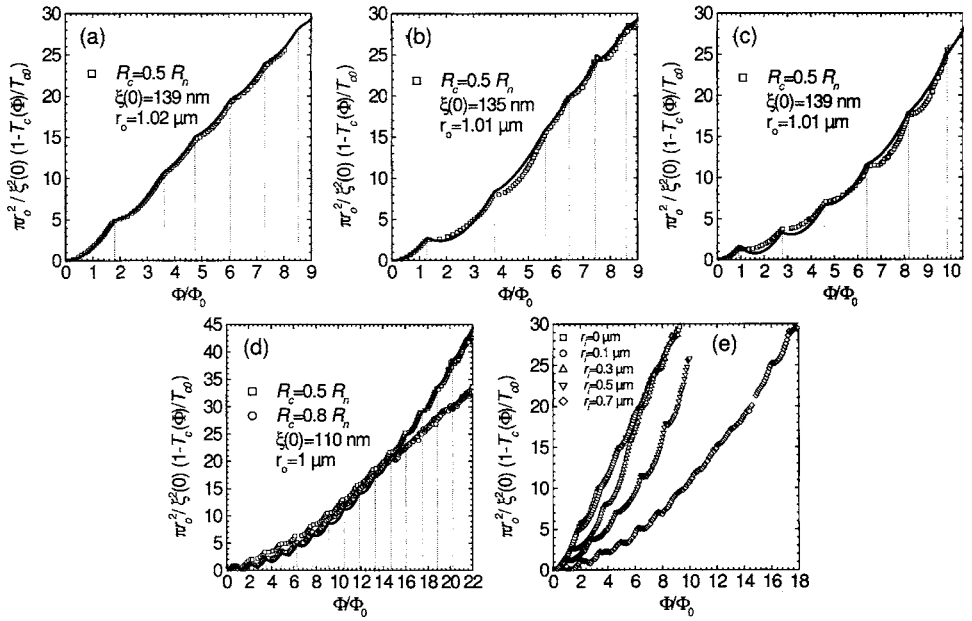

FIG. 34. The $T_c(H)$ phase boundary of a loop with inner to outer radius ratio (a) $x=0.1$, (b) $x=0.3$, (c) $x=0.5$, and (d) $x=0.7$. The open squares [and the open circles in (d)] represent the measured data. The solid lines are the calculated $E_{\mathrm{LLL}}(H)$. The experimental $T_c(H)$ phase boundaries of the different structures are compared in (e).

fields. There, the situation is reversed. A sharp transition is first observed, followed by a broad transition at low resistance. We will show below that the broad transition also corresponds to the nucleation in the wedges. This effect is observed in a broader magnetic field range when the ratio x increases.

D. $T_c(H)$ phase boundaries

The experimental phase boundary of the disk has already been presented in Fig. 21. The data for the ring with $x=0.1$ are shown in Fig. 34(a). The flux Φ on the field axis denotes the flux $\Phi=\mu_0 H\pi r_o^2$ through the ring and the hole. The H–T diagram of the ring with the smallest hole resembles strongly the $T_c(H)$ line of the disk displayed in Fig. 21. The phase boundary has a linear background superimposed with oscillations. A very good agreement between the measured and the calculated curves is found.

Figure 34(b) shows the H–T diagram of the ring with $x=0.3$. Here, the linear dependence is only seen for vorticity $L>4$. At lower magnetic field, a parabolic background suppression of T_c is observed. The crossover from the linear to the parabolic regime occurs at $\pi r_o^2/\xi^2(T)\approx 20$. This corresponds to a value $r_o-r_i\approx 1.8\ \xi(T)$, which is in a good agreement with the thickness $\tau=1.84\ \xi(T)$ for a crossover from a one-dimensional (1D) to a 2D regime for a thin film in a parallel magnetic field.[57,58]

A good agreement with the position of the cusps in the theoretical curve has been found. The amplitude of the oscillations in the experimental curve deviates slightly from the calculated one. At $L=1$, between the first and the second $T_c(H)$ cusps, the experimental oscillation is less pronounced. For higher vorticity, the opposite situation is seen where the amplitude of the experimental oscillations is larger than in the theoretical curve.

The penetration of the first vortex in the ring occurs at a lower magnetic field value than for the ring with the smallest hole [see Fig. 34(a)], while the transitions $L=1\leftrightarrow 2$ to $L=5\leftrightarrow 6$ occur at a higher magnetic field. That the transitions take place at lower magnetic field value for a ring with thinner lines is expected since the transition between L and $L+1$ occurs at $\Phi/\Phi_0=L+1/2$ for an infinitely thin loop or cylinder. At higher magnetic fields, a giant vortex state is formed[53] and the

disk with a small hole in the center behaves like the disk without hole. This, however, cannot fully explain why the change in vorticity is delayed at high magnetic fields by introducing a small hole in a disk.

The measured $T_c(H)$ phase boundary of the ring with ratio $x=0.5$ is shown in Fig. 34(c). In the temperature range accessible with our experimental setup, only a parabolic background dependence of the critical temperature on the magnetic field has been measured. By comparing the experimental results with the calculations, a similar behavior as for the ring with $x=0.3$ is seen. The position of the cusps in the experimental curve matches with the calculated transitions. However, no good agreement is found for the amplitude of the oscillations. For the vorticities $L=1$ and 2, the amplitude is lower in the experimental curve, while for $L>3$, the amplitude is larger. At low L, the transition between states with different vorticities occurs at a lower magnetic field than for the disk, while the transitions $L=3\leftrightarrow 4$, $L=4\leftrightarrow 5$ and $L=5\leftrightarrow 6$ take place at a higher magnetic field, similar to what was observed for the ring with $x=0.3$.

The H–T diagram of the ring with the thinnest line ($x=0.7$) is shown in Fig. 34(d). Two experimental curves are presented, one for $R_c=0.5R_n$ (open squares) and the second for $R_c=0.8R_n$ (open circles). It can be seen that at a higher resistance criterion the parabolic dependence switches to a linear regime at high magnetic field. For the curve calculated with the low resistance criterion, a quasiparabolic background suppression of $T_c(H)$ is observed over the whole measured range. The amplitude of the $T_c(H)$ oscillations is larger than in the samples with smaller x and the transition between states with different vorticities is almost periodic in field. A good agreement between the theoretical curve and the experimental curve with $R_c=0.5R_n$ is seen at high magnetic fields. At lower magnetic fields, a good agreement is found when using a higher resistance criterion.

The phase boundaries of the four different loops are compared with the critical temperature of the disk in Fig. 34(e). All the curves overlap with each other for $L=0$. *It is interesting to note that an opening in the disk does not affect the phase boundary as long as no vortex is trapped inside the superconductor*. Only the magnetic field range over which the state with $L=0$ exists at the phase boundary is lowered by introducing a hole in the disk. The $T_c(H)$ line of the disk with the smallest hole in the middle does not deviate substantially from the phase boundary of the disk without any opening. Only small changes in the position of the cusps is observed at low vorticity. For larger holes, the crossover from 2D to 1D regime is clearly seen. The samples with the thinnest lines do not show the 2D regime in the studied temperature interval and only the parabolic dependence is seen.

In order to reveal the origin of this different behavior at low and high magnetic field, a contour plot of the resistance $R(H,T)$ is presented in Fig. 35. Two different parts are clearly distinguished. Below 10 mT, the low resistance is linear, while the high resistance exhibits a parabolic background superimposed with oscillations. Above 10 mT, the opposite situation occurs, where the low resistance has a parabolic decay with small oscillations while the high resistance decreases monotonously. The parabolic part coincides with the nucleation of superconductivity in the loop shown as a full line. The linear part arises from the nucleation in the wedge contacts.

By fitting the theoretical critical temperature of a wedge with opening angle $\Gamma=15°$ to the linear part of the contour plot (dashed line), a coherence length $\xi(0)=140$ nm is obtained. This differs from the coherence length $\xi(0)=110$ nm that was used to find a good agreement between the experiment and the theoretical curve of a loop. A possible origin of this discrepancy could be a width of the loop that has been evaluated to be smaller than the real size. An estimate of the thickness that would satisfy the coherence length used for the calculation of the wedge contacts can be obtained from the analysis of the nucleation field of a thin wire of a film in a parallel magnetic field. From the calculation of the nucleation field of a thin film in a parallel field,[52] a value for the width of the loop of 0.38 μm is obtained instead of 0.3 μm found from SEM measurements. This difference is too large to be explained only by an error in the characterization of the sample. The opening angle of the contacts can be determined with a high accuracy so that a divergence arising from a wrong determination of Γ could be excluded. It means that either the nucleation of superconductivity is delayed in the wedges due to the presence of the loop or that the

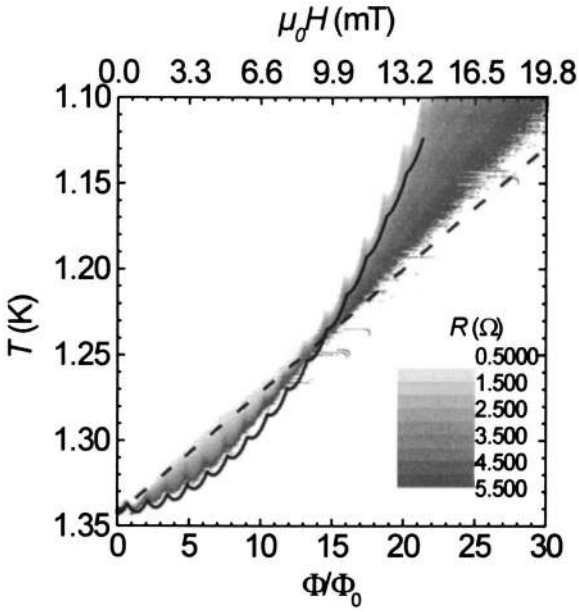

FIG. 35. Contour plot of the resistance $R(H,T)$ of a loop with $x=0.7$. The full line represents the calculated phase boundary of a loop with $r_i=0.7$ μm and $r_o=1$ μm, using a coherence length of 110 nm. The dashed line is the theoretical critical temperature of a wedge with opening angle $\Gamma=15°$ with $\xi=140$ nm.

nucleation in the loop is enhanced by the contacts. It is also possible that the coherence length in the loop is slightly different from that in the wedge. The sample geometry can indeed affect the superconducting parameters λ and ξ in a structure of mesoscopic size similar to the case of a thin film where the effective penetration depth increases as $\lambda'=\lambda^2/\tau$, taking into account the demagnetization effects. The renormalization of λ and ξ should therefore be calculated in a self-consistent way from the sample geometry.

The shape of the resistive curves in Fig. 33 can be easily understood from Fig. 35. It was clearly seen that in low magnetic fields the nucleation first occurs in the ring and is then followed by the nucleation in the contacts. Due to the different field dependence of the $T_c(H)$ of the ring and the contacts, the opposite occurs in higher magnetic fields. Two different shapes are therefore distinguished in the resistive curves depending on the part where superconductivity starts to nucleate. The same happens in the rings with $x=0.3$ and $x=0.5$ since T_c also has a parabolic field dependence for low fields. The normal parts of the sample can however partially become superconducting by the proximity effect with the neighboring superconducting part.

VI. STABILITY OF THE LGL SOLUTIONS AND THE PHASE TRANSITIONS BELOW THE NUCLEATION TEMPERATURE

The lowest level E_{LLL} of the LGL equation, describing the nucleation of superconductivity in applied magnetic field, $T_c(H)$, is always nondegenerate for finite size samples.[59] Therefore the corresponding solution is fully consistent with the symmetry of the sample in applied field as we have seen in the preceding section. This is opposite to the case of bulk type-II superconductors without boundaries, where $E_{\mathrm{LLL}}(H)$ is an infinitely degenerate Landau level while the nucleating order parameter is a combination of its degenerate components,[42] always of broken symmetry (BS) type. Besides the symmetry, the discreteness of the spectrum of the LGL equation in mesoscopic superconductors implies the stability of the shape of the nucleated order parameter in a range of temperatures close to the $T_c(H)$ line. Such stability of a symmetric order parameter has been found for mesoscopic cylinders,[30,34,40,60,61] squares and triangles.[62–66] Remarkably, a similar phenomenon is encountered in molecular physics where it is known as the pseudo-Jahn-Teller effect.[67]

In this section we investigate the mechanisms of phase transitions from a nucleated order parameter of a mesoscopic superconductor to another symmetry or broken symmetry phase when temperature is lowered.[68] We find that in the case of BS phase transitions most often only one single LGL solution of different symmetry effectively admixes to the nucleated phase. In this case the description of the phase transition is equivalent to the description of vibronic instability in a simple (two-level) pseudo-Jahn-Teller problem. Such analogy is specific to mesoscopic superconductors, which have discrete LGL spectrum, and gives a "molecular" view on the mechanism of BS phase transitions in mesoscopic samples. We also investigate the existence of different phases as a function of the samples size and find that the region on the phase diagram corresponding to the nucleated order parameter of S solution increases with reducing the size. The critical sizes, corresponding to the disappearence of BS phase transitions (when the nucleated S phases persist down to $T=0$) are predicted to be in the range of micrometers for conventional superconductors, i.e., within the reach of current experimental techniques. This opens possibilities for the experimental verification of different transitions predicted here on the basis of the similarities with pseudo-Jahn-Teller mechanism.

As before we consider a superconducting polygon of size a (a^2 is the surface of the sample) and thickness d in a perpendicular uniform magnetic field H. For small ($a \sim \xi$, the coherence length) and thin ($d \ll \xi$) samples one can neglect the variation of the order parameter across thickness[30,40] and the distortion of the magnetic field induced by screening and vortex currents. The order parameter Ψ is found from the minimization of the two-dimensional GL functional,

$$\Delta F = \int \left[\alpha |\Psi|^2 + \frac{1}{2}\beta |\Psi|^4 + \frac{1}{2m^*} \left| \left(-i\hbar \nabla - \frac{2e}{c}\mathbf{A} \right) \Psi \right|^2 \right] \mathrm{d}S, \tag{63}$$

with the boundary condition (7). Minimizing (63) without the term $\sim|\Psi|^4$ results in the linear eigenvalue equation (4) with the solutions which we further denote by ϕ_i, ϵ_i. The lowest solution ϕ_1 describes the nucleation phase boundary via the equation $\epsilon_1 = -\alpha$. The eigenvalues ϵ_i, measured in units of $\hbar^2/2m^* a^2 (\epsilon_i')$, depend only on the applied magnetic flux $\Phi = Ha^2$, presented in units of the superconducting flux quantum Φ_0. The eigenstates of (34), normalized to unity within the surface of the sample, are used further as the basis set for the order parameter,

$$\Psi = \sum_{i=1}^{N} c_i \phi_i, \tag{64}$$

where N is the dimension of the basis set. Substitution of (64) into (63) yields ΔF as a function of the expansion coefficients

$$\Delta F = \sum_i \alpha_i |c_i|^2 + \frac{\beta}{2a^2} \sum_{ijkl} A_{ij}^{kl} c_i^* c_j^* c_k c_l,$$

$$\alpha_i \equiv \alpha + \epsilon_i, \tag{65}$$

where the parameters

$$A_{ij}^{kl} = a^2 \int \phi_i^* \phi_j^* \phi_k \phi_l \, \mathrm{d}S \tag{66}$$

depend only on the geometry but not on the size of the sample. A_{ii}^{ii} is precisely the Abrikosov parameter β_A[69] for the state ϕ_i, which is a measure of its "flatness."

The actual parameters defining the relative free energy in Eq. (65) can be found as follows. If we use coefficients $c_i \to a\sqrt{-\alpha_1/\beta} c_i$ and measure the free energy in units of $a^2\alpha_1^2/\beta$ (α_1 corresponds to the lowest LGL eigenvalue ϵ_1) then the right-hand side of Eq. (65) will depend (besides

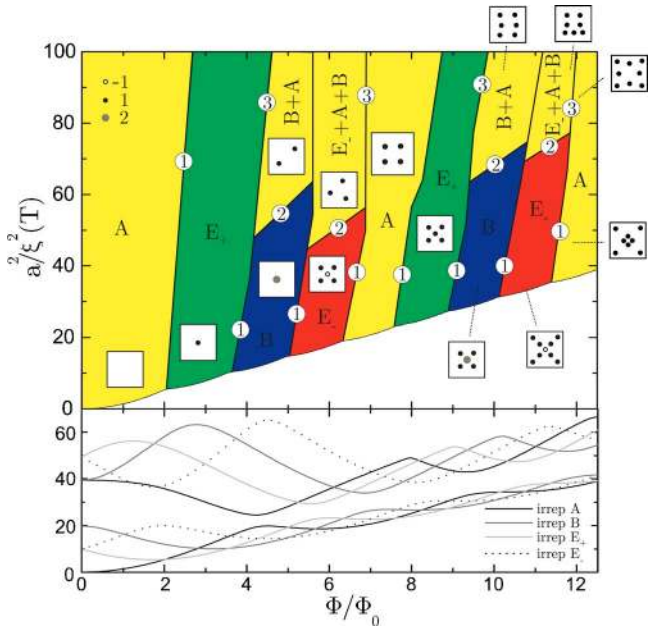

FIG. 36. (Color online) Lower panel, LGL solutions ϵ_i' for a square with superconductor-vacuum boundary condition, characterized by irreps A ($m=0$), B ($m=2$), E_+ ($m=1$), and E_- ($m=-1$). Upper panel, the corresponding phase diagram obtained by Monte Carlo calculations. For each phase, the vortex structure is shown schematically and the involved irreps are indicated. The number at each boundary line denotes the type of transition (Table II). In the color online version: the colors stand for the winding number of the central vortex: 0 (yellow), 1 (green), 2 (blue), and −1 (red).

A_{ij}^{kl}) only on the ratios $\alpha_i/\alpha_1=(a^2/\xi^2+\epsilon_i')/(a^2/\xi^2+\epsilon_1')$. Hence the GL functional for a given sample (measured in units of $a^2\alpha_1^2/\beta$) and the emerging phase diagram are only dependent on $(a/\xi(T))^2$ and Φ/Φ_0.

As we have already seen (Figs. 11 and 12), the spectrum of eigenvalues of the LGL equation is strongly influenced by the symmetry of the problem. If the sample has a rotational symmetry axis C_n, the Landau levels are split in groups of n levels belonging to different irreps, because only these can intersect each other. In addition, the C_n symmetry imposes the selection rules on integrals in Eq. (66), $m_k+m_l-m_i-m_j=0$, similar to the case of cylindrical symmetry.[34,60]

Because the fourth order terms in (65) are overall positive, it is generally expected that only the states ϕ_i with $\alpha_i<0$ will effectively contribute to the order parameter. In the close vicinity to the nucleation phase boundary only α_1 is negative, therefore $\Psi\approx c_1\phi_1$, with $c_1=a\sqrt{-\alpha_1/\beta A_{11}^{11}}$ $\sim\sqrt{(a/\xi)^2-\epsilon_1'}$ and the free energy $\Delta F_1=-(\alpha_1^2/2\beta A_{11}^{11})a^2$. The only allowed admixtures in this phase are from the excited LGL states of the same irrep, $\phi_{1'}$, described by the coefficients $c_{1'}$,

$$\frac{c_{1'}}{c_1}\approx-\frac{A_{11'}^{11}c_1^2}{\alpha_{1'}/\beta+[2A_{11'}^{11'}+|A_{11'}^{11}|\cos(\chi_{1'1'}^{11}-2\chi_{11'}^{11})]c_1^2}, \tag{67}$$

where $\chi_{ij}^{kl}=\arg A_{ij}^{kl}$. In the temperature region where $\alpha_{1'}>0$ the coefficients $c_{1'}$ in (67) show smooth behavior, with continuous derivatives with respect to temperature. The symmetry-preserving phase transitions can therefore occur only when some of $\alpha_{1'}$ become negative. However in symmetric samples the ϕ_i states which are close to ϵ_1 are always of different symmetry (lower panel in Fig. 36) so that many of the corresponding parameters α_i will become negative before $\alpha_{1'}$. We can conclude that the nucleated order parameter will undergo a phase transition *modifying its symmetry* when temperature is lowered.

Even if there are many LGL states with $\alpha_i<0$ at a given temperature, only a few of them actually contribute to the order parameter. This is due to the fact that while the terms $\sim A_{ii}^{ii}$ and $\sim A_{ii}^{jj}$ give net contributions to "repulsion," the other terms, which could become negative, partially

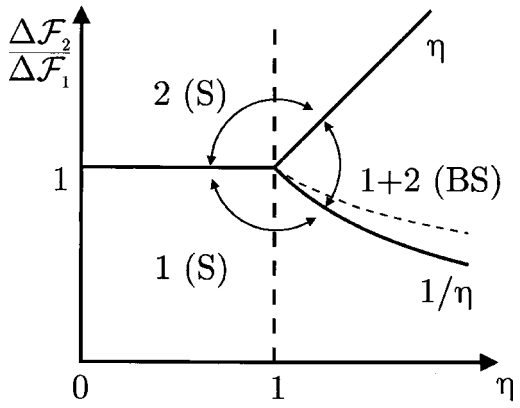

FIG. 37. Diagram of thermodynamically stable phases (solid lines) for the effective two-state model (68) as a function of the parameters from Eqs. (69) and (70). 1, 2 are pure phases and 1+2 is the mixed one.

cancel out when N is increased. One can check indeed that already for $N>3$ there are less available phases of complex c_i coefficients than A_{ij}^{kl} terms to be optimized. The mutual reduction of these terms increases with the number of mixed LGL states which means that at a certain value of N further admixture will become unfavorable. It is expected therefore that only a few different irreps will effectively admix at the transition point.

Next we adopt a general description of the phase transitions from a nucleated order parameter, which is achieved by the following consideration. Given the small number of different irreps among the states ϕ_i which admix at the transition point, we can always divide the corresponding $\{c_i\}$ in two groups so as to bring the functional (65) to the following basic form:

$$\Delta F = \tilde{\alpha}_1 c_1'^2 + \tilde{\alpha}_2 c_2'^2 + \frac{\beta}{2a^2}(A_{11}c_1'^4 + A_{22}c_2'^4 + 2A_{12}c_1'^2 c_2'^2), \tag{68}$$

where c_1' and c_2' are the norms of the coefficients in the first and the second group, respectively, while the parameters $\tilde{\alpha}_1$, $\tilde{\alpha}_2(<0)$ and A_{11}, A_{22}, $A_{12}(>0)$ are functions of associated angular variables to be specified below. The two groups contain different irreps, in numbers n_1 and n_2, correspondingly (ϕ_1 belongs to the first group). Minimization with respect to c_1' and c_2' for fixed values of the five parameters in (68) results in three (meta)stable phases,

$$\Delta F_1 = -\frac{\tilde{\alpha}_1^2}{2\beta A_{11}}a^2, \quad \Delta F_2 = -\frac{\tilde{\alpha}_2^2}{2\beta A_{22}}a^2,$$

$$\frac{\Delta F_{12}}{\Delta F_1} = \frac{(\sqrt{\eta \Delta F_2/\Delta F_1} - 1)^2}{\eta - 1} + 1, \tag{69}$$

where

$$\eta = \frac{A_{11}A_{22}}{A_{12}^2}. \tag{70}$$

The first two are pure phases, with $c_2'=0$ and $c_1'=0$, respectively, while ΔF_{12} is the mixed one $(c_1', c_2' \neq 0)$. Figure 37 shows the diagram of the thermodynamically stable phases. The vertical line $\eta=1$ divides the diagram in two regions. On the left-hand side we have a switch between pure phases (first-order transition). On the right-hand side the two phase boundary lines correspond to the second order transitions. At temperatures close to the lower phase boundary, $T=T_{\mathrm{BS}}-\Delta T$, $\xi=\xi_{\mathrm{BS}}-\Delta\xi$, the BS phase will grow as $c_2' \sim \sqrt{\Delta T}$, $\sqrt{\Delta\xi}$.

Now the free energy expressions (69) are minimized with respect to the remaining variables from $\tilde{\alpha}_i$ and A_{ij} resulting in the lowest energy phase for a given temperature. Since we are looking for phase transitions from the nucleated S-order parameter, the pure phase 1 in Fig. 37 always corresponds to ϕ_1 with possible small admixtures of the same symmetry, Eq. (67). Depending on the symmetries of other LGL states which admix through the transition we can have several types of phase transitions which are investigated below. As in the case of ϕ_1, the contributions from states of other symmetries are mainly represented by one LGL state. Therefore to simplify further analysis we will consider that only one state per irrep contributes.

In the case of a single admixed state (ϕ_2) one should substitute $c_1=c_1'$ and $c_2=c_2'$ in Eq. (68) and $\tilde{\alpha}_i=\alpha_i$, $A_{ii}=A_{ii}^{ii}$ and $A_{12}=2A_{12}^{12}-|A_{11}^{22}|$ into (69) and (70). When the interaction between these states, A_{12}, is larger than $\sqrt{A_{11}^{11}A_{22}^{22}}$, the order parameter corresponds either to ϕ_1 or ϕ_2 (left-hand side of the diagram in Fig. 37). The transition from ϕ_1 to ϕ_2 takes place when

$$\frac{\alpha_2}{\alpha_1} > \sqrt{\frac{A_{22}^{22}}{A_{11}^{11}}}. \tag{71}$$

The left-hand side of this equation increases with lowering the temperature, being always <1. Therefore the transition between symmetric states can only occur if $A_{22}^{22}<A_{11}^{11}$. When the interaction is weaker, $\eta>1$, the transition from ϕ_1 to a BS order parameter (right-hand side of the phase diagram) can arise under the condition

$$\frac{\alpha_2}{\alpha_1} > \frac{A_{12}}{A_{11}^{11}}. \tag{72}$$

When two states of different symmetry mix with ϕ_1, two situations can occur.

(1) If the involved irreps obey the inequalities $m_1+m_3-2m_2\neq 0,\pm n$, $m_1+m_2-2m_3\neq 0,\pm n$, then one has $c_1=c_1'$, $c_2=c_2'\cos\varphi$, $c_3=c_2'\sin\varphi$, and

$$\tilde{\alpha}_1=\alpha_1,$$

$$\tilde{\alpha}_2=\alpha_2\cos^2\varphi+\alpha_3\sin^2\varphi,$$

$$A_{11}=A_{11}^{11},$$

$$A_{22}=A_{22}^{22}\cos^4\varphi+A_{33}^{33}\sin^4\varphi+(A_{23}^{23}-|A_{22}^{33}|/2)\sin^2 2\varphi,$$

$$A_{12}=2A_{12}^{12}\cos^2\varphi+2A_{13}^{13}\sin^2\varphi-|A_{11}^{23}|\sin 2\varphi, \tag{73}$$

Substituting (73) into Eqs. (69) and minimizing with respect to φ we obtain again three thermodynamically stable phases of Fig. 37 for corresponding equilibrium values of φ. The difference is that now the left-hand side of the diagram describes the switch between the symmetric (ϕ_1) and the broken-symmetry ($\phi_2+\phi_3$) phases, while the BS phase on the right-hand side of the diagram corresponds to $\phi_1+\phi_2+\phi_3$.

(2) If the first or the second relation for irreps becomes equality then $c_1=c_1'\cos\varphi$, $c_2=c_2'$, $c_3=c_1'\sin\varphi$, or $c_1=c_1'\cos\varphi$, $c_2=c_1'\sin\varphi$, $c_3=c_2'$, respectively. Therefore for $\eta<1$ we can only have a symmetry-changing transition from ϕ_1 to ϕ_2 (or ϕ_3). However for $\eta>1$, at φ corresponding to thermodynamically stable BS phase $\phi_1+\phi_2+\phi_3$, the lowest boundary line in Fig. 37 separates this phase from the metastable one $\phi_1+\phi_3$ (or $\phi_1+\phi_2$). Therefore the phase transition from ϕ_1 will take place along the line which lies somewhere higher (dashed line in Fig. 37), i.e., it is of the first order. This type of transition is associated with a small jump of c_1, hence it is close to second order.

TABLE II. Possible transitions from a symmetric vortex phase.

Type[a]	η	n_1	n_2	n_f[b]	Order (symmetry)
1	<1	1	1	1	I (S)
2	>1	1	$\geqslant 1$	n_2+1	II (BS)
3	<1	1	>1	n_2	I (BS)
4	>1	>1	$\geqslant 1$	n_2+n_1	I (BS)

[a]Numbers used in Fig. 36.
[b]Number of irreps in the final state.

Considering higher numbers of mixing irreps will not result in qualitatively new phase transitions which are thus of four types (Table II).

The diagram of the lowest transitions from symmetric phases in a thin square was evaluated within the above approach, which compares well with an accurate Monte Carlo calculation[70] shown in the upper panel of Fig. 36. The critical values of ξ calculated by the two approaches differ by only several percents. One finds indeed that only a few states effectively admix to the order parameter. The described region in the phase diagram becomes relatively large with decreasing a. For small enough samples some phase boundary lines pass above $(a/\xi(0))^2$ and the nucleated symmetric phases remain thermodynamically stable down to $T=0$. Thus the transition from the phase with an antivortex in the center ($\Phi/\Phi_0=5.5\leftrightarrow 6.5$) to a BS phase with the same vorticity but without antivortex is suppressed for $a<(7\leftrightarrow 8)\xi(0)$ (≈ 1 μm for Al).

It follows from Fig. 36 that the phase boundary lines separating the areas with different vorticity have positive slopes and correspond to transitions of type 1 (Table II) in the lower part of the diagram.[71] The reason is the increase of Abrikosov parameters β_A in the lowest group of LGL states (Fig. 36) when passing through the corresponding avoided crossings towards increased fields. Indeed, it was shown[24] that the lowest Landau level of each irrep maps into cylindrical states with rotational numbers L to the left and $L+n$ to the right of the avoided crossing, respectively. Therefore for two lowest LGL states the Abrikosov parameter is smaller for the ground state to the left and for the excited one to the right of their intersection, so that the condition (71) can only be obeyed in the latter case.

On the other hand, the obtained transitions to broken-symmetry phases are always of the second order and go mostly via a two-state mixing scenario (in the phases E_-+A+B in Fig. 36 the admixture of B states is relatively small). The direct analogy for this in molecular physics is the pseudo-Jahn-Teller (PJT) instability of symmetric geometry of a molecule with respect to a low symmetry nuclear distortion (q). Usually such an instability results from a strong interaction of the ground electronic state (ϕ_1) with an excited state (ϕ_2), induced by q, which is described by the Hamiltonian,[67]

$$H_{\mathrm{PJT}}=\frac{1}{2}Kq^2+\begin{pmatrix}-\Delta & V_q\\ V_q & \Delta\end{pmatrix}, \tag{74}$$

where 2Δ is the energy gap between the ground and the excited states in the symmetric nuclear configuration, V is the vibronic constant, and K is the force constant. The instability occurs when $V^2/K>\Delta$ and it results in an equilibrium distortion $q^{(0)}$ (Fig. 38) and a broken-symmetry electronic ground state.

The PJT instability can be described by considering a functional depending on electronic variables only.[72] To obtain such a functional, we average H_{PJT} over $\Psi=c_1\phi_1+c_2\phi_2$, find the equilibrium value of q as function of c_1 and c_2 and substitute it back into the average,

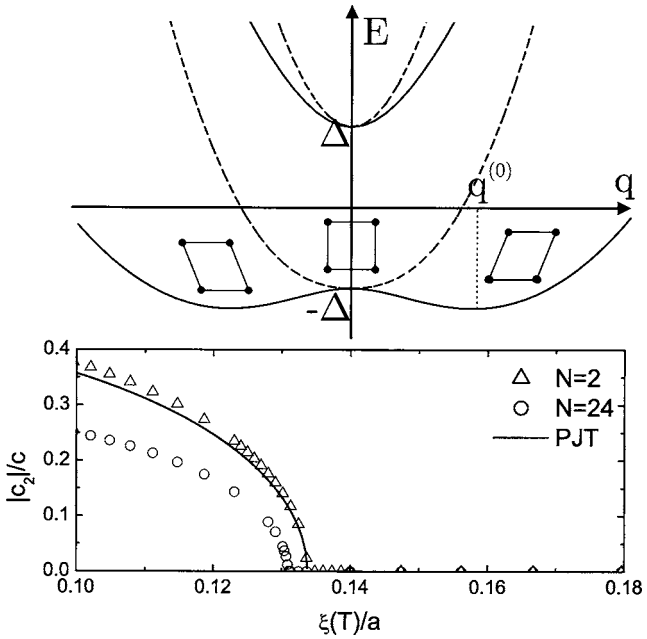

FIG. 38. Upper panel, adiabatic potential for two nondegenerate electronic terms of a square molecule in the case of weak (dashed lines) and strong (solid lines) pseudo-Jahn-Teller effect. Lower panel, temperature dependence of the normalized coefficient of admixture of the excited (A) state close to the $B \rightarrow B+A$ transition at $\Phi=4.5\Phi_0$ (Fig. 36) evaluated by Monte Carlo calculations and the pseudo-Jahn-Teller effect using the correspondence relations (77). The numbers in the inset denote the dimension of the basis set in the Monte Carlo calculations.

$$\langle \Psi | H_{\mathrm{PJT}} | \Psi \rangle^0 = -\frac{2V^2}{K} c_1^2 c_2^2 + \Delta(-c_1^2 + c_2^2). \tag{75}$$

Next we introduce polar coordinates, $c_1=c\cos\varphi$, $c_2=c\sin\varphi$ for the PJT functional (75) and $c_1=A_{11}^{-1/4}c\cos\varphi$, $c_2=A_{22}^{-1/4}c\sin\varphi$ for the functional (68), where φ plays now the role of the order parameter for the BS state. The φ-dependent part of both functionals has now the following common form:

$$\Delta E(\varphi) = -Ac^4 \sin^2 2\varphi - Bc^2 \cos^2\varphi, \tag{76}$$

where $A=V^2/2K$, $B=\Delta$ for the PJT problem and $A=(\beta/4a^2)(1-\eta^{-1/2})$, $B=(\alpha_2 A_{22}^{-1/2}-\alpha_1 A_{11}^{-1/2})/2$ for the case of superconductor. The main difference between them is that $c=1$ in the former and $c\neq 1$ in the second case. Therefore the correspondence between PJT and GL parameters is the following:

$$V^2/K \rightarrow \frac{|\alpha_1|}{2\sqrt{A_{11}}}\left(1-\frac{1}{\sqrt{\eta}}\right),$$

$$2\Delta \rightarrow \frac{\alpha_2}{\sqrt{A_{22}}} - \frac{\alpha_1}{\sqrt{A_{11}}}. \tag{77}$$

Lower panel in Fig. 38 shows how the broken symmetry phase appears for vortex molecules. We can see that the evolution of the order parameter with temperature is reproduced by the pseudo-Jahn-Teller effect. In the case $N=2$, only the ground B and the first excited A LGL states are taken into account. The accurate calculation involving $N=24$ LGL states shifts the transition point obtained in the $N=2$ calculation only by $\approx 2\%$. This shift mainly arises due to the renormalization of the effective parameters in Eq. (68) when more LGL states are taken into account.

As a result of this renormalization the nucleated phase becomes optimized so that the transition takes place at a lower temperature compared to the two-state approximation.

As the analysis shows the specific structural similarity between the pseudo-Jahn-Teller and GL symmetry breaking mechanisms is due to the presence of a quartic dependence on the expansion coefficients. A different mechanism of symmetry breaking was described by Berger for the case of the Schrödinger equation for a cylinder.[73] In this case breaking of axial symmetry was obtained through the induced magnetic field and the quadratic term in the GL potential was not considered.

The symmetric order parameters are found to be remarkably stable below the nucleation temperature, which is a pure mesoscopic effect. Besides, the mesoscopic samples show a rich variety of vortex phases compared to bulk type II superconductors where only the Abrikosov vortex lattice occurs. By using an effective two-state model the nature of the transition to these phases has been revealed and four distinct types of transitions have been found. The symmetry-breaking phase transition has the same structure as the pseudo-Jahn-Teller instability of high symmetry nuclear configurations in molecules. This analogy provides an interesting connection between real and vortex molecules.

The existence of phases can be experimentally verified by using various local probe techniques such as Hall probe microscopy, STM and AFM. The phase diagram is found to be strongly dependent on the samples size. In particular, the region on the phase diagram corresponding to the nucleated (symmetric) order parameter enlarges with reducing the size of the sample. The critical size corresponding to the complete disappearance of the BS phase (the nucleated *S*-phase persists until $T=0$) is predicted to be of the order of micrometers for conventional superconductors, such as Al, Pb. These predictions can be checked experimentally on different mesoscopic superconducting systems.

VII. CONCLUSIONS

An analytical gauge transformation for the vector potential is derived with a vanishing normal component at the boundary line of any regular polygon. With this vector potential gauge, the linearized Ginzburg–Landau problem reduces to an eigenvalue equation in a basis set of functions obeying Neumann boundary conditions, which can be found for different regular polygons. The proposed approach allows for accurate evaluations of the order parameter distributions and proves to be especially efficient at moderate values of applied magnetic fields. For low values of applied magnetic fluxes the order parameter for superconducting square and equilateral triangle contains an antivortex in the center. These solutions are found to be stable with respect to small deviations from the phase boundary line and can be probed by techniques which are sensible to the superfluid density, for example, by using scanning tunnelling microscopy. The calculated lowest energy levels $E_{\mathrm{LLL}}(H)$ show a very good agreement with the measured phase boundaries $T_c(H)$ for a variety of different geometries (triangles, squares, disks, rectangles, loops). By using full GL equations symmetry-breaking transitions deeper in the superconducting state have been studied. A remarkable similarity of these transitions for vortex molecules with pseudo-Jahn-Teller effect for real molecules has been revealed.

ACKNOWLEDGMENTS

This work is supported by the Flemish Science Fund (FWO) and the K.U. Leuven Concerted Action Scheme (GOA), by the IUAP network of the Belgian Government, and by the ESF AQDJJ Programme. One of the authors (M.M.) acknowledges support from the Institute for the Promotion of Innovation through Science and Technology in Flanders (IWT-Vlaanderen). One of the authors (C.C.) acknowledges financial support from Fundación Ramón Areces (Spain) through Post-Doctoral Studentship Grants and from MAT2004-04364 (Spain).

[1] V. V. Moshchalkov, L. Gielen, C. Strunk, R. Jonckheere, X. Qiu, C. Van Haesendonck, and Y. Bruynseraede, Nature (London) **373**, 319 (1995).
[2] V. L. Ginzburg and L. D. Landau, Zh. Eksp. Teor. Fiz. **20**, 1064 (1950).

[3] P.-G. de Gennes, *Superconductivity of Metals and Alloys* (Benjamin, New York, 1966).
[4] J. T. Devreese, Physica C **332**, 242 (2000).
[5] F. M. Peeters, V. A. Schweigerdt, B. J. Baelus, and P. S. Deo, Physica C **332**, 255 (2000).
[6] D. Saint-James, G. Sarma, and E. J. Thomas, *Type II Superconductivity* (Pergamon, Oxford, 1973).
[7] A. Houghton and F. B. McLean, Phys. Lett. **19**, 172 (1965).
[8] V. M. Fomin, J. T. Devreese, and V. V. Moshchalkov, Europhys. Lett. **42**, 553 (1998).
[9] D. Saint-James, Phys. Lett. **15**, 13 (1965).
[10] H. J. Fink and A. G. Presson, Phys. Rev. **151**, 219 (1966).
[11] V. V. Moshchalkov, X. G. Qiu, and V. Bruyndoncx, Phys. Rev. B **55**, 11793 (1997).
[12] P. S. Deo, V. A. Schweigert, F. M. Peeters, and A. K. Geim, Phys. Rev. Lett. **79**, 4653 (1997).
[13] L. D. Landau and E. M. Lifshitz, *Theory of Fields* (Mir, Moscow, 1970).
[14] G. A. Korn and T. M. Korn, *Mathematical Handbook for Scientists and Engineers* (McGraw-Hill, New York, 1968).
[15] L. F. Chibotaru, A. Ceulemans, G. Teniers, V. Bruyndoncx, and V. V. Moshchalkov, Eur. Phys. J. B **27**, 341 (2002).
[16] *Handbook of Mathematical Functions*, edited by M. Abramowitz and I. Stegun (Dover, New York, 1970).
[17] D. S. Golubović, W. V. Pogosov, M. Morelle, and V. V. Moshchalkov, Europhys. Lett. **65**, 546 (2004).
[18] M. V. Miloševič and F. M. Peeters, Phys. Rev. B **68**, 094510 (2003).
[19] L. D. Landau and E. M. Lifshitz, *Electrodynamics of Continuum Media* (Mir, Moscow, 1969).
[20] C. Carballeira, L. F. Chibotaru, A. Ceulemans, and V. V. Moshchalkov (unpublished).
[21] L. D. Landau and E. M. Lifshitz, *Quantum Mechanics*, 2nd ed. (Pergamon, Oxford, 1975).
[22] W.-K. Li and S. M. Blinder, J. Math. Phys. **26**, 2784 (1985).
[23] J. W. Turner, J. Phys. A **17**, 2791 (1984).
[24] L. F. Chibotaru, A. Ceulemans, M. Lorenzini, and V. V. Moshchalkov, Europhys. Lett. **63**, 159 (2003); **63**, 476(E) (2003).
[25] L. F. Chibotaru, A. Ceulemans, V. Bruyndoncx, and V. V. Moshchalkov, Phys. Rev. Lett. **86**, 1323 (2001).
[26] L. F. Chibotaru, A. Ceulemans, V. Bruyndoncx, and V. V. Moshchalkov, Nature (London) **408**, 833 (2000).
[27] H. T. Jadallah, J. Rubinstein, and P. Sternberg, Phys. Rev. Lett. **82**, 2935 (1999).
[28] R. Benoist and W. Zwerger, Z. Phys. B: Condens. Matter **103**, 377 (1997).
[29] R. B. Dingle, Proc. R. Soc. London, Ser. A **211**, 500 (1952).
[30] V. A. Schweigert, F. M. Peeters, and P. S. Deo, Phys. Rev. Lett. **81**, 2783 (1998).
[31] J. J. Palacios, Phys. Rev. B **58**, R5948 (1998).
[32] G. M. Bravermans, S. A. Gredeskul, and Y. Avishai, Phys. Rev. B **59**, 12039 (1999).
[33] A. I. Buzdin and J. P. Brison, Phys. Lett. A **196**, 267 (1994).
[34] J. J. Palacios, Physica B **256–258**, 610 (1998).
[35] E. Akkermans and K. Mallick, J. Phys. A **32**, 7133 (1999).
[36] A. P. van Gelder, Phys. Rev. Lett. **20**, 1435 (1968).
[37] V. A. Schweigert and F. Peeters, Phys. Rev. B **60**, 3084 (1999).
[38] F. Brosens, J. T. Devreese, V. M. Fomin, and V. V. Moshchalkov, Solid State Commun. **111**, 565 (1999).
[39] S. N. Klimin, V. M. Fomin, J. T. Devreese, and V. V. Moshchalkov, Solid State Commun. **111**, 589 (1999).
[40] V. A. Schweigert and F. M. Peeters, Phys. Rev. B **57**, 13817 (1998).
[41] B. J. Baelus, S. V. Yampolskii, and F. M. Peeters, Phys. Rev. B **66**, 024517 (2002).
[42] A. A. Abrikosov, *Fundamentals of the Theory of Metals* (North-Holland, Amsterdam, 1988).
[43] J. Bonca and V. V. Kabanov, Phys. Rev. B **65**, 012509 (2002).
[44] M. Morelle, G. Teniers, L. F. Chibotaru, A. Ceulemans, and V. V. Moshchalkov, Physica C **369**, 351 (2002).
[45] M. Morelle, Y. Bruynseraede, and V. V. Moshchalkov, Phys. Status Solidi B **237**, 365 (2003).
[46] V. Bruyndoncx, J. G. Rodrigo, T. Puig, L. V. Look, V. V. Moshchalkov, and R. Jonckheere, Phys. Rev. B **60**, 4285 (1999).
[47] O. Buisson, P. Gandit, R. Rammal, Y. Y. Wang, and B. Pannetier, Phys. Lett. A **150**, 36 (1990).
[48] G. Teniers, L. F. Chibotaru, A. Ceulemans, V. V. Moshchalkov, Europhys. Lett. **63**, 296 (2003).
[49] T. Schuster, M. V. Indenbom, M. R. Koblischka, H. Kuhn, and H. Kronmüller, Phys. Rev. B **49**, 3443 (1994).
[50] E. H. Brandt, Phys. Rev. B **52**, 15442 (1995).
[51] T. Schuster, H. Kuhn, and E. H. Brandt, Phys. Rev. B **54**, 3514 (1996).
[52] M. Tinkham, *Introduction to Superconductivity* (McGraw-Hill, New York, 1975).
[53] V. Bruyndoncx, L. V. Look, M. Verschuere, and V. V. Moshchalkov, Phys. Rev. B **60**, 10468 (1999).
[54] A. Bezryadin, A. I. Buzdin, and B. Pannetier, Phys. Lett. A **195**, 373 (1994).
[55] A. Bezryadin and B. Pannetier, J. Low Temp. Phys. **98**, 251 (1995).
[56] M. Morelle, D. S. Golubović, and V. V. Moshchalkov, Phys. Rev. B **70**, 144528 (2004).
[57] H. A. Schultens, Z. Phys. **232**, 430 (1970).
[58] H. J. Fink, Phys. Rev. **177**, 732 (1969).
[59] Except for the points of accidental degeneracy where levels of different symmetry intersect.
[60] J. J. Palacios, Phys. Rev. Lett. **84**, 1796 (2000).
[61] G. F. Zharkov, Phys. Rev. B **63**, 224513 (2001).
[62] L. F. Chibotaru, A. Ceulemans, G. Teniers, and V. V. Moshchalkov, Physica C **369**, 149 (2002).
[63] T. Mertelj and V. V. Kabanov, Phys. Rev. B **67**, 134527 (2003).
[64] B. J. Baelus and F. M. Peeters, Phys. Rev. B **65**, 104515 (2002).
[65] A. S. Mel'nikov, I. M. Nefedov, D. A. Ryzhov, I. A. Schereshevskii, V. M. Vinokur, and P. P. Vysheslavtsev, Phys. Rev. B **65**, 140503 (2002).
[66] V. R. Misko, V. M. Fomin, J. T. Devreese, and V. V. Moshchalkov, Phys. Rev. Lett. **90**, 147003 (2003).

[67] I. B. Bersuker and V. Z. Polinger, *Vibronic Interactions in Molecules and Crystals* (Springer, Berlin, 1989).
[68] L. F. Chibotaru, G. Teniers, A. Ceulemans, and V. V. Moshchalkov, Phys. Rev. B **70**, 094505 (2004).
[69] A. A. Abrikosov, Sov. Phys. JETP **5**, 1174 (1957).
[70] G. Teniers, V. V. Moshchalkov, L. F. Chibotaru, and A. Ceulemans (unpublished).
[71] Interestingly, phase boundary lines with *negative* slopes have been found for a thin superconducting film with a circular hole; A. Bezryadin, A. Buzdin, and B. Pannetier, Phys. Rev. B **51**, 3718 (1995).
[72] A. Ceulemans, J. Chem. Phys. **87**, 5374 (1987).
[73] J. Berger, Phys. Rev. B **63**, 172507 (2001).